



PERGAMON

Progress in Particle and Nuclear Physics 43 (1999) 419–483

---

Progress in  
Particle and  
Nuclear Physics

---

<http://www.elsevier.nl/locate/pnpartnuclphys>

## The Origin of the Heavy Elements: The *s* Process

F. KÄPPELER

*Forschungszentrum Karlsruhe, Institut für Kernphysik, D-76021 Karlsruhe, Germany*

### Abstract

The heavy elements with  $Z \geq 30$  are made in about equal quantities by neutron capture reactions during stellar He burning and presumably in supernovae. This contribution deals mainly with the slow neutron capture (*s*) process which is responsible for about one half of the abundances in the mass region between Fe and Bi. The slow time scale implies that the reaction path of this process involves mostly stable isotopes which can be studied in detail in laboratory experiments. Based on these data, the quantitative interpretation of the natural abundances provides an exciting possibility for exploring a variety of problems related to stellar and Galactic evolution. The *p* process, which provides a very small but significant admixture to many of the *s* abundances, has recently attracted increasing interest as a possibility for supernova studies.

*Key words:* stellar nucleosynthesis, neutron capture reactions, *s* process, *p* process

### Contents

1	Introduction	1
2	The observed abundances	4
2.1	The composition of the solar system	4
2.2	Astronomical observations	6
3	Neutron capture nucleosynthesis	7
4	Stellar helium burning and the <i>s</i> process	9
4.1	Nuclear physics: measurements and theoretical aspects	10
4.2	The canonical <i>s</i> process	27

*Preprint submitted to Elsevier Preprint*

*4 March 1999*

0146-6410/99/\$ - see front matter © 1999 Elsevier Science BV. All rights reserved.

PII: S0146-6410(99)00098-8

4.3	Stellar <i>s</i> -process models	34
4.4	Abundances: <i>s</i> -process yields and <i>r</i> -process residuals	41
4.5	Comparison with observations	43
5	Explosive scenarios and the <i>p</i> nuclei	46
5.1	The <i>r</i> -process nucleosynthesis	46
5.2	The <i>p</i> process	46
6	Nuclear chronometers	50
6.1	Time scales for the <i>s</i> process	51
6.2	Chronometers for explosive nucleosynthesis	52
7	Open problems	53
	References	54

## 1 Introduction

During human history, the quest for the origin of matter was always a fascinating subject of philosophical and theological debates. The first experimental steps into this up to then rather speculative field started not before the middle of last century. Strolling through the main street of Heidelberg may bring you to Nr. 59, where the sign shown in Fig. 1 marks the birthplace of modern astrophysics.

Spectral analysis was the first physics technique to be applied in astronomy and it turned into a remarkable success story. It allowed to explain the Fraunhofer lines in the solar spectrum, within short it led to the safe classification of stars, and - almost exactly a century after the discovery of the Fraunhofer lines - to the Hertzsprung-Russell diagram in 1913.

The quantitative interpretation of the Fraunhofer lines as a signature for the chemical composition remained, however, a tantalizing problem. First theories of stellar atmospheres became available in the late twenties but still at present such analyses are affected by uncertainties of typically 20 - 30%. Nevertheless, these studies showed that most stars have elemental compositions which are very similar to that of the Sun. Accordingly, the solar abundance distribution was sometimes referred to as the "cosmic" abundance distribution.



Fig. 1. The inscription at the house Nr. 59 in the main street of Heidelberg reminds us of the birthplace of modern astrophysics: *In 1859 Kirchhoff has applied in this house his spectral analysis which he developed with Bunsen to the Sun and to stars and made thus the chemistry of the Universe accessible.*

Another search for the chemical composition of the Sun started with studies of terrestrial rocks. When these studies failed due to chemical differentiation in the earth's crust, interest focused on meteorites, which were considered sufficiently primitive as to represent the original composition of the protosolar nebula. After a first systematic tabulation by Goldschmidt [1], this approach became the basis for nucleosynthesis studies mainly by the work of Suess and Urey [2] and Cameron [3] in the fifties.

An important complement to the reliable determination of the solar abundance distribution were extensive studies of stellar atmospheres. Refined observations in the fifties revealed significant abundance differences between the Sun and different types of stars, in particular the chemically peculiar red giant stars. In fact, the discovery of Tc lines in the spectra of a certain class of these stars [4] became a decisive argument in favor of stellar nucleosynthesis, since this element has no stable isotopes and, therefore, must have been produced within these stars (Sec. 4.5). In view of this more complex picture, the term cosmic distribution is certainly not appropriate for the solar composition.

While the abundance compilations were an essential basis, the formulation of our present-day picture of nucleosynthesis would not have been possible without the rapid development of nuclear physics, which provided the ultimate answer with respect to the stellar energy source via the pp-chain [5] and the CNO cycle [6,7] as well as the key to identify and interpret the various sites and processes responsible for the cosmic production of the chemical elements.

Merging these fields, namely the elemental composition of astronomical objects, the standard abundance distribution describing the isotopic composition, and the related nuclear physics, was the great achievement of the fundamental paper by Burbidge, Burbidge, Fowler, and Hoyle or B<sup>2</sup>FH for short [8]. This work set the stage for Nuclear Astrophysics, a whole new field of research, which brought forth a wealth of ideas and results. Many of these aspects were

also formulated in a parallel analysis of Cameron [9].

There are a number of review articles dealing with the various topics of Nuclear Astrophysics. A comprehensive summary of the 40 years of progress in nucleosynthesis since B<sup>2</sup>FH was published recently by Wallerstein et al. [10]. Many reviews on the origin of the heavy elements appeared in the past decade, either providing an overview [11,12] or dealing with particular nucleosynthesis scenarios [13–21].

The present attempt concentrates on the origin of the heavy elements between Fe and Bi. Unlike the more abundant light elements, the heavies are not produced by fusion of charged particles but are the result of neutron reactions. This article starts out in Sec. 2 with the observed abundances, featuring the signatures of the various processes of nucleosynthesis, followed in Sec. 3 by an overview of the different modes of heavy element nucleosynthesis. In Sec. 4 the slow neutron capture process or *s* process is presented in some detail. This discussion includes the determination of the relevant neutron capture cross sections and stellar  $\beta$ -decay rates, the canonical *s*-process approaches as well as an account of current models for stellar He burning.

All other contributions to the heavy element abundances are coming from explosive scenarios, i.e. from the *r*, *p*, and *rp* processes. This implies that nuclear reaction rates exceed the  $\beta$ -decay rates by orders of magnitude, resulting in complex reaction networks near the drip lines. As outlined in Sec. 5, the rapid neutron capture process (*r* process) is the second dominant mechanism for the abundances in the mass region  $A > 60$ . In this case, laboratory approaches are yet limited, but are important to guide theoretical extrapolations of the relevant nuclear physics to the very neutron rich nuclei of the actual *r*-process region. This section describes also the minor abundance component by the *p* process, which had to be postulated to explain the existence of the rare, proton rich nuclei, which are not accessible by neutron capture reactions.

The article ends with a description of potential nuclear chronometers (Sec. 6) and with a brief summary of the remaining problems (Sec. 7).

## 2 The observed abundances

The credibility of any nucleosynthesis model must be checked against observations. Naturally, the composition of the solar system was considered a suited test for this purpose. The choice of the Sun as a standard offers the advantage that its composition can be derived via spectroscopy of the photosphere as well as by analysis of meteorites, primarily of type C1 carbonaceous chondrites. As indicated before, notations such as *standard* or even *cosmic* abundance distri-

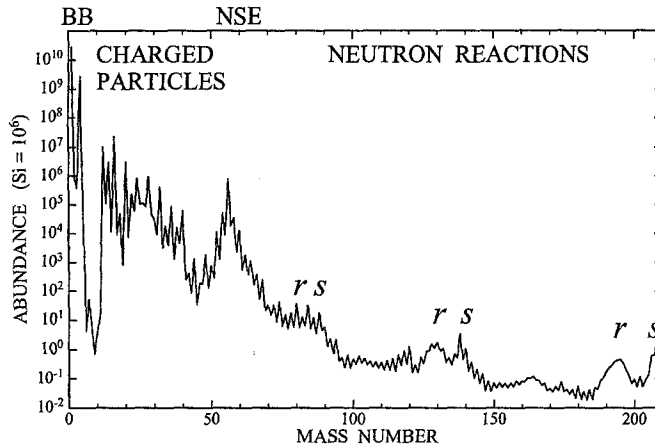


Fig. 2. The isotopic abundance distribution in the solar system (from Ref.[23]).

bution should be used with caution, however. Although the Sun seems to be a fairly normal main sequence star with a composition similar to a characteristic average it has to be understood that a truly standard chemical composition does not exist at any point in time [22].

### 2.1 *The composition of the solar system*

The solar abundance distribution is the only complete sample with a well defined isotopic composition. This is important since the isotopic abundances are reflecting the nucleosynthesis reactions. The plot of Fig. 2 shows the latest compilation of Ref.[23] and illustrates the signatures of several scenarios. The distribution is clearly dominated by the primordial H and He abundances from the Big Bang, followed by the deep minimum at the rare and fragile elements Li, Be, and B, which are difficult to produce because of the stability gaps at  $A=5$  and  $8$ , but are easily burnt in stars. Probably, the present abundances were produced by Galactic cosmic rays via spallation reactions [24].

Stellar nucleosynthesis starts with  $^{12}\text{C}$  and  $^{16}\text{O}$  produced during He burning, which are partly converted to  $^{14}\text{N}$  by the CNO cycle in later stellar generations. In subsequent stages of stellar evolution, the light elements up to the mass 40 to 50 region are produced by charged particle reactions during C, Ne, and O burning [10]. The corresponding yields show a strong preference for the most stable nuclei built from  $\alpha$ -particles. This part of the distribution is strongly influenced by the Coulomb barrier, resulting in an exponential decrease with increasing atomic number  $Z$ .

Ultimately, Si burning leads to such high temperatures that nuclear statistical equilibrium (NSE) is reached. Under these conditions, only the most stable

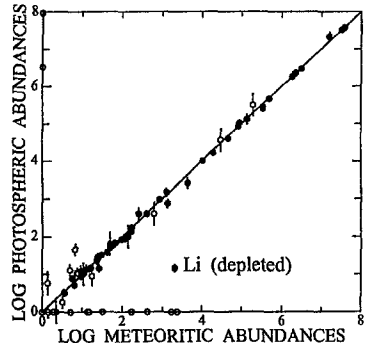


Fig. 3. For all elements, where reliable analyses can be performed, the photospheric and meteoritic abundance data are in good agreement (solid circles) [22].

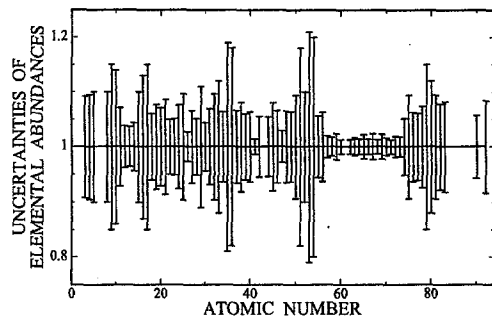


Fig. 4. The uncertainties of the elemental abundances derived from meteorite analyses are typically 5 to 10 %, but note the important exception of the lanthanides. Data are from Ref. [26].

nuclei around Fe are abundantly produced [25], giving rise to the outstanding abundance maximum at  $A=56$ . From this point on, further build-up of heavier nuclei by charged particle reactions ceases due to the increasing Coulomb barriers and the decreasing binding energies per nucleon.

Accordingly, all remaining abundances up to the actinides are essentially shaped by neutron capture nucleosynthesis, leading to a fairly flat distribution characterized by the pronounced  $r$  and  $s$  maxima. These twin peaks are the signatures of the slow ( $s$ ) and rapid ( $r$ ) neutron capture processes discussed in Sec. 3.

The remarkable progress in defining the solar abundance distribution is illustrated in Figs. 3 and 4. Based on more accurate atomic data the photospheric abundances could be improved considerably and are now in good agreement with the respective meteoritic values [22], at least for those elements, where reliable analyses can be performed. Apart from the better atomic data, this improvement over the rather uncertain situation a decade ago (e.g. Fig. 6 in Ref.[13]) is due to progress in observations, where high quality data from the UV to the far IR became available as well as in modelling the photosphere. Despite of several yet uncertain values (open circles in Fig. 3) it is now generally accepted [22] that the solar photosphere and the C1 carbonaceous chondrites have exactly the same composition.

Therefore, most elemental and practically all isotopic abundances are derived from meteorites. Recent compilations of such data [22,23,26] agree within  $\pm 3\%$ , a clear improvement compared with the corresponding tables of 1982 [27] and 1973 [28] which differed by some 20 %. However, Fig. 4 illustrates that typical uncertainties in the elemental composition are still between 5 and 10 %. Only for Fe, Nb, Ag, and the group of the rare earth elements (REE) rather

accurate abundances can be quoted, which bear important consequences for neutron capture nucleosynthesis in He burning scenarios (Secs. 4.2 to 4.4).

As far as the isotopic abundance patterns are concerned, there is perfect agreement between terrestrial and meteoritic data on average. However, fascinating anomalies have been discovered in meteoritic inclusions, which were identified as pristine material from various nucleosynthesis sites (Sec. 4.5). Furthermore, it is worth noting that isotopic patterns in terrestrial material may exhibit significant scatter as a result of differentiation [29]. For example, the  ${}^6\text{Li}$  component of natural Li may show variations of several percent, clearly a problem that needs to be considered in sample preparations for accurate cross section measurements (Sec. 4.1.2).

In summary, the consolidation of the solar abundance distribution provides a reliable basis for the quantitative discussion of various nucleosynthesis scenarios.

## 2.2 *Astronomical observations*

Over the last two decades the development of new equipment (spectrometers and detectors) and improved theoretical tools (model atmospheres and synthetic spectrum calculations) have led to considerable progress in the spectroscopy of astronomical objects. Therefore, this technique represents an essential source of information for our understanding of stellar and Galactic evolution, e.g. via studies along the asymptotic giant branch (AGB) [30,31] and of the abundance distributions in very old stars [32,33]. Observations in the infrared allow to study the composition of planetary nebulae [34] and circumstellar envelopes [35], UV absorption line diagnostics yields the composition of interstellar matter [36], while X-ray [37] and  $\gamma$ -ray astronomy [38] have produced exciting new views on explosive nucleosynthesis [39,40].

With respect to the origin of the heavy elements, observations of *s*-process abundances in AGB stars and of the *r*-process patterns in very metal poor stars are most important.

As mentioned before, it was the 1952 discovery of Tc lines in red giant stars of spectral type S by Merrill [4], that provided a decisive argument in favor of stellar nucleosynthesis. Ever since, spectral observations of peculiar red giants turned out to be a prolific source of information for the He burning stage of stellar evolution [41]. As discussed in Sec. 4.5, the *s*-process material, which is produced in the He-burning zones of red giant stars and then efficiently transported to the surface by deep convective motions, provided important clues for the yet uncertain models of these stars.

Since red giants are cool enough for the most refractive chemical compounds to form, even isotopic yields can be determined for some elements, e.g. Mg [42] and Zr [43], with direct implications for the *s*-process neutron source and the related neutron density. Recently, it has been shown that high resolution spectroscopy allows to deduce isotopic abundances via line broadening due to the hyperfine splitting. First measurements of this effect [44,45] produced controversial results, which relate to the question whether the heavy elements in metal-poor stars exhibit really an *r*-process abundance pattern as suggested in Ref. [46].

### 3 Neutron capture nucleosynthesis

The concept of neutron capture reactions in stars as the origin of the heavy elements has been first formulated in the fifties by B²FH and by Cameron [8,9] with the distinction of a slow and a rapid process.

Most of the relevant features were already considered in these early works, starting from the stellar  $(n,\gamma)$  cross sections as the important nuclear physics input, over the Ansatz for the canonical *s*-process model and the neutron sources in the helium burning zones to the observations of *s*-enhancements in stellar atmospheres. At that time, evidence for an *s* process associated with stellar He burning came from the Tc observations of Merrill [4], from the sharp maxima in the abundance distribution of Fig. 2, and from isobaric abundances.

The last two features imply also the existence of two more nucleosynthesis mechanisms in addition to the *s* process. This is illustrated in Fig. 5, which shows the respective reaction paths in the chart of nuclides.

Since the *s* process operates at relatively low neutron densities, neutron capture times are much longer than typical  $\beta$ -decay half-lives. Therefore, the *s*-process reaction path follows the stability valley as indicated by the solid line in Fig. 5. The developing *s* abundances are determined by the respective  $(n,\gamma)$  cross sections averaged over the stellar neutron spectrum, such that isotopes with small cross sections are building up large abundances. In particular, small cross sections are characteristic for nuclei with closed neutron shells N=50, 82, and 126, which correspond to the sharp *s*-process maxima in the abundance distribution at A=88, 140, and 208.

This behavior represents a first example for the intimate correlation between the observed abundances and the physical conditions during nucleosynthesis. Accordingly, the abundance pattern allows for rather sensitive and detailed tests of nucleosynthesis scenarios, provided that the information preserved in the abundances can be deciphered. This important aspect will repeatedly be

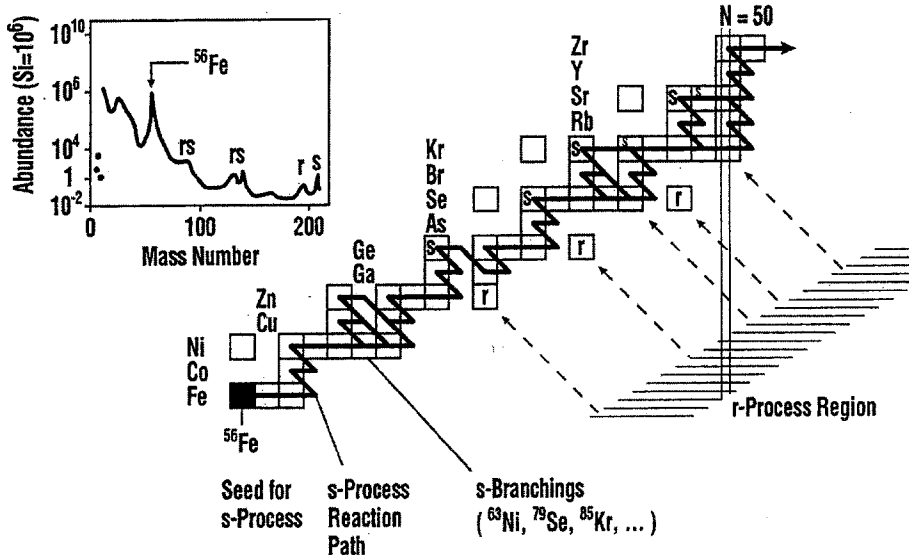


Fig. 5. An illustration of the neutron capture processes responsible for the formation of the nuclei between iron and the actinides. The observed abundance distribution in the inset shows characteristic twin peaks. These peaks result from the nuclear properties where the *s*- and *r*-reaction paths encounter magic neutron numbers. Note that a *p* process has to be invoked for producing the proton rich nuclei that are not reached by neutron capture reactions. (For details see discussion in text.)

emphasized throughout this review.

The *r*-process counterparts of these maxima are caused by the effect of neutron shell closure on the  $\beta$ -decay half-lives. Since the *r* process occurs in regions of extremely high neutron density (presumably during stellar explosions in supernovae, see the contribution by Haxton and Qian in this volume), neutron captures are much faster than  $\beta$ -decays. This drives the *r*-process path off the stability valley to where the neutron separation energies are only  $\approx 2$  MeV. At these points,  $(n,\gamma)$  and  $(\gamma,n)$  reactions are in equilibrium, and the reaction flow has to wait for  $\beta$ -decay to the next higher element. Therefore, the *r* abundances are proportional to the half-lives of these waiting point nuclei. This means that abundance peaks accumulate again at neutron magic nuclei, but at lower mass numbers compared the related *s*-process maxima. The corresponding twin peaks are marked in the abundance distribution given in the inset of Fig. 5 and in Fig. 2. The separation of these abundance peaks indicates the intersection of the *r*-process path with the respective magic neutron numbers.

While the observed abundances are dominated by the *s* and *r* components, which both account for approximately 50% of the abundances in the mass re-

gion  $A > 60$ , the rare proton-rich nuclei cannot be produced by neutron capture reactions. This minor part of the abundance distribution had to be ascribed to the  $p$  process that is assumed to occur in explosively burning outer shells of supernovae (Sec. 5).

Naturally, the  $s$  process is more easily accessible to laboratory experiments as well as to stellar models and astronomical observations [13]. Attempts to describe the  $r$  and  $p$  processes are hampered by the large uncertainties in the nuclear physics data far from stability [16], but also - and perhaps more severely - by the problems related to a detailed modelling of stellar explosions [47–49]. These difficulties are best illustrated by the fact that the actual site of both processes has not yet been reliably identified.

Obviously most isotopes received abundance contributions from the  $s$  and the  $r$  process. But as indicated in Fig. 5, there are neutron-rich stable isotopes (marked  $r$ ) that are not reached by the  $s$  process because of their short-lived neighbors. Consequently, this species is of pure  $r$  process origin. In turn, these  $r$ -only nuclei terminate the  $\beta$ -decay chains from the  $r$ -process region, making their stable isobars an ensemble of  $s$ -only isotopes. The existence of these two subgroups is of vital importance for nucleosynthesis, since the credibility of any model depends on how well the abundances of these particular nuclei can be reproduced.

#### 4 Stellar helium burning and the $s$ process

The time scale for neutron capture being slower than the average  $\beta$ -decay half-lives constrains the reaction path of the  $s$  process to follow the valley of  $\beta$ -stability. It is impressive to remember that most of the related consequences had been derived already 40 years ago by B<sup>2</sup>FH, who clearly identified the product of the stellar cross section times the resulting abundance,  $\langle\sigma(A)\rangle N_s(A)$  as the characteristic quantity of the  $s$  process. Two different  $s$ -process components were inferred from the observed abundance distribution, and the *local approximation*

$$\langle\sigma N\rangle_A = \text{const.}$$

was discussed as being due to reaction equilibrium in mass regions between magic neutron numbers. Furthermore, the information that can be deduced from branchings in the reaction path was recognized as an important means for  $s$ -process studies. However, quantitative conclusions could not be obtained at that time, mostly due to severe uncertainties in the stellar  $(n, \gamma)$  cross sections.

With the continuous improvement of these cross sections, the validity of the concept suggested by B<sup>2</sup>FH was confirmed. In particular, analysis of the

branchings in the reaction path turned out to be significant for the role of the *s* process with respect to stellar models. Such branchings occur when the neutron capture chain encounters isotopes with  $\beta$ -decay half-lives that are comparable to the neutron capture times. The resulting competition between  $\beta$ -decay and neutron capture causes the *s*-process path to split, e.g. at  $^{79}\text{Se}$ , and  $^{85}\text{Kr}$  in Fig. 5. Apart from the neutron capture cross sections and  $\beta$ -decay half-lives, the strength of these branchings can best be derived from the abundances of the involved *s*-only isotopes, such as  $^{80}\text{Kr}$  and  $^{86}\text{Sr}$  in the above examples. The abundance patterns of the branchings are essentially determined by the neutron flux and the temperature at the *s*-process site and, hence, carry detailed information on the physical conditions in the stellar plasma (Sec. 4.2.2).

#### *4.1 Nuclear physics: measurements and theoretical aspects*

The main nuclear physics input for *s*-process studies are the  $(n,\gamma)$  cross sections of all nuclei along the reaction path from Fe to Bi as well as the  $\beta$ -decay rates at the branching points.

Neutron physics in the astrophysically relevant energy regime from about 0.1 keV to a few hundred keV has reached a relatively mature stage. The advent of suited accelerators and detector technologies led to the present situation where the stellar  $(n,\gamma)$  rates for *s*-process applications start to be reliable enough for interpreting the observed abundance patterns as a critical test for models of stellar helium burning. If current efforts in this field will be pursued for another decade, the quality of these data may have reached a satisfactory level, where *s*-process analyses are no longer limited by the cross section uncertainties.

An important nuclear physics aspect, that was not anticipated by B<sup>2</sup>FH, was the enhancement of  $\beta$ -decay rates at stellar temperatures. In typical *s*-process environments, such enhancements result from transitions between low-lying nuclear states, which are thermally populated by the hot photon bath. So far, theoretical estimates for this possibility could be tested by a limited number of experiments. In view of its importance for the interpretation of *s*-process branchings, this field should be considered with renewed interest.

##### *4.1.1 Laboratory neutron sources*

Though produced with high initial energies predominantly in the exothermic ( $\alpha,n$ ) reactions on  $^{13}\text{C}$  and  $^{22}\text{Ne}$ , stellar neutrons are quickly thermalized under *s*-process conditions. According to the range of thermal energies from  $\approx 8$  keV in low mass stars to 80 keV during carbon burning in massive stars, laboratory

studies of stellar  $(n,\gamma)$  cross sections cover the neutron energy range up to a few hundred keV.

Neutrons in the keV range are produced in several ways: nuclear reactions, such as  $^7\text{Li}(\text{p},\text{n})^7\text{Be}$  in connection with low-energy particle accelerators, offer the possibility of tailoring the neutron spectrum exactly to the energy range of interest; this has the advantage of low backgrounds. Therefore, comparably short neutron flight paths can be used in these cases which compensate to a certain extent the limitations in neutron flux. This approach is followed, for example, at the pulsed electrostatic accelerators in Karlsruhe [13] and Tokyo [50].

Much higher intensities can be achieved at linear accelerators via  $(\gamma,\text{n})$  reactions by bombarding heavy metal targets with electron beams of typically 50 MeV. When these very energetic neutrons are slowed down by a moderator the resulting spectrum contains all energies from thermal to near the initial electron energy. Since the astrophysically relevant energy range corresponds only to a small window in the entire spectrum, background conditions are more complicated and measurements need to be carried out at larger neutron flight paths. In turn, the longer flight paths are advantageous for high resolution measurements which are important in the resonance region. Accelerators of this type are ORELA in Oak Ridge, Tennessee and GELINA in Geel, Belgium. Examples of recent astrophysical measurements at these facilities are described in Refs. [51] and [52], respectively.

Spallation reactions induced by energetic particle beams provide the most prolific sources of fast neutrons. An advanced spallation source suited for neutron time-of-flight (TOF) work is the LANSCE facility at Los Alamos, where the primary proton beam from a linear accelerator is accumulated in an external storage ring from where intense bursts with a repetition rate of only 12 Hz can be extracted. This results in extremely favorable signal-to-background ratios, allowing for measurements on very small samples as well as on radioactive targets [53]. Even higher neutron fluxes are anticipated for the spallation source at the CERN-PS, which is now under construction and will operate with a repetition rate of 0.4 Hz [54]. Plans for a TOF facility are also discussed for the proposed Oak Ridge spallation source.

Thermal reactors do also play a certain role in this type of measurements. With neutron filters quasi-monoenergetic spectra suited for cross section measurements can be produced in the keV range [55]. This application is particularly useful for determining the energy dependence of partial cross sections to isomeric states. Another aspect of reactor measurements relates to the fact that thermal cross sections are rather well known. If measurements at stellar energies are repeated at thermal energies by using the same setup and the same samples, the cross section can be normalized at the respective thermal value.

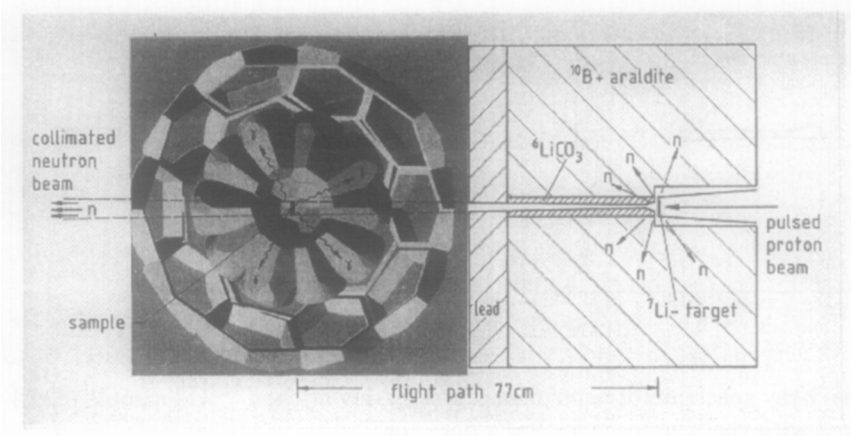


Fig. 6. The Karlsruhe  $4\pi$   $\text{BaF}_2$  detector.

In this way, systematic uncertainties in detection efficiency and sample mass can be eliminated [56].

#### 4.1.2 Neutron capture cross sections

**Time-of-flight measurements:** The experimental methods for measuring  $(n,\gamma)$  cross sections fall into two groups, TOF techniques and activations. TOF techniques are applicable to all stable nuclei. Such measurements require a pulsed neutron source for determining the neutron energy via the flight time between neutron production target and capture sample. Capture events are identified by the prompt  $\gamma$ -ray cascade in the product nucleus.

The best signature for the identification of neutron capture events is the total energy of the  $\gamma$ -cascade by which the product nucleus deexcites to its ground state. Hence, accurate measurements of  $(n,\gamma)$  cross sections are best to be made by using a detector that operates as a calorimeter with good energy resolution. In the  $\gamma$ -spectrum of such a detector, all capture events would fall in a line at the neutron binding energy (typically between 5 and 10 MeV), well separated from the  $\gamma$ -ray backgrounds that are inevitable in neutron experiments, and independent of the multiplicity of the  $\gamma$ -ray cascade.

These arguments point to a  $4\pi$  detector of high efficiency, made of a scintillator with reasonably good time and energy resolution. In addition, the detector should be insensitive to scattered neutrons, since - on average - the scattering cross sections are about 10 to 100 times larger than the capture cross sections. These aspects have been combined in the design of the Karlsruhe  $4\pi$   $\text{BaF}_2$  detector [57], which consists of 42 individual  $\text{BaF}_2$  crystals forming a spherical shell of  $\text{BaF}_2$  with 15 cm thickness and 20 cm inner diameter as sketched in Fig. 6.

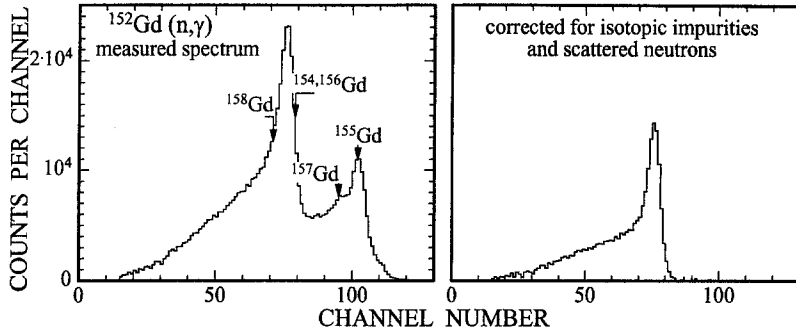


Fig. 7. The  $\gamma$ -ray spectrum of neutron captures in an enriched  $^{152}\text{Gd}$  sample (32%) as measured with the Karlsruhe  $4\pi \text{ BaF}_2$  detector.

The essential features of this detector are a resolution in  $\gamma$ -ray energy ranging from 14% at 662 keV to 6% at 6.13 MeV, a time resolution of 500 ps, and a  $\gamma$ -ray efficiency of better than 90% in the energy range below 10 MeV. This means that capture events can indeed be detected as a line at the binding energy. This is illustrated in Fig. 7 at the example of a recent measurement on the  $s$ -only isotopes  $^{152}\text{Gd}$  and  $^{154}\text{Gd}$ , which define the branchings at  $A=151/154$  [58]. Though the line shape exhibits a significant tail due to the fact that a few  $\gamma$ -rays escape detection, the resolution is sufficient to distinguish background events from isotopic impurities and to check the respective corrections. From this spectrum the efficiency for capture events was determined to be  $98.0 \pm 0.7\%$ , which represents the major contribution to the resulting cross section uncertainty of 1%.

The differential data,  $\sigma(E_n)$ , obtained in TOF experiments are then folded with the Maxwellian neutron spectra for various stellar temperatures to determine the effective stellar cross sections,

$$\langle \sigma v \rangle_{kT} = \frac{\langle \sigma v \rangle}{v_T} = \frac{2}{\sqrt{\pi}} \frac{\int_0^\infty \sigma(E_n) \times E_n \times \exp(-E_n/kT) dE_n}{\int_0^\infty E_n \times \exp(-E_n/kT) dE_n},$$

$v_T$  denoting the mean thermal velocity [13].

In general, the Maxwellian averaging for the "standard" thermal energy of  $kT = 30$  keV requires data in the energy range from a few keV up to  $\sim 200$  keV. Recent stellar models suggest, however, that the  $s$  process may partly operate at much lower temperatures corresponding to  $kT=8$  keV, which means that stellar cross sections are also affected by contributions from lower energies. This aspect is particularly important for nuclei at or near magic neutron numbers which exhibit a pronounced resonance structure due to the small level density. Such data are the domain of TOF measurements at moderated sources, which can be carried out with high resolution.

Alternative detection methods for neutron capture events based on  $\gamma$ -ray de-

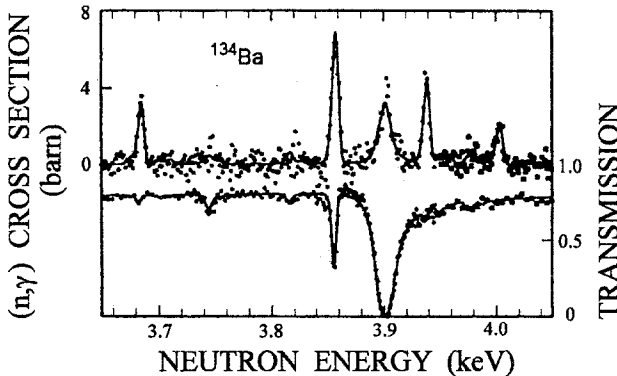


Fig. 8. High resolution capture (top) and transmission data (bottom) for  $^{134}\text{Ba}$  measured at ORELA [51].

tectors with low efficiency have to correct for the multiplicities of the  $\gamma$ -ray cascades, either through the intrinsic detector properties in case of Moxon-Rae type detectors [59] or by an off-line pulse height weighting technique, which is commonly used at moderated neutron sources (see e.g. Refs. [51,52]). Resonance analyses of such high resolution data are facilitated if the capture measurement is complemented by a transmission experiment that yields the total reaction cross section and the neutron widths of the resonances. This is illustrated in Fig. 8 showing capture and transmission data for  $^{134}\text{Ba}$  from a measurement at ORELA [51].

Other examples of this type - both for the  $\gamma$ -detection based on  $\text{C}_6\text{D}_6$  liquid scintillator counters in combination with the pulse height weighting technique as well as for the astrophysical relevance - are the measurements on  $^{138}\text{Ba}$  and  $^{208}\text{Pb}$  at the GELINA accelerator [52]. Two new resonances in  $^{138}\text{Ba}$  below 2 keV neutron energy were observed in this experiment, resulting in a significantly larger cross section at low *s*-process temperatures than expected before. Since the small cross sections of neutron magic isotopes govern the reaction flow to heavier nuclei, this has an important impact on the *s*-process abundance distribution.

Both experimental approaches imply the use of isotopically enriched samples. In this respect, the higher  $\gamma$ -efficiency of the  $4\pi \text{ BaF}_2$  detector has the advantage that 5 to 10 times smaller sample masses can be used compared with other detector types.

In contrast to the statistically randomized  $\gamma$ -ray cascades emitted in neutron captures on intermediate and heavy nuclei, well defined cascades with a few, separated  $\gamma$ -transitions are observed in light isotopes due to the much lower level densities. Based on this feature, the very small  $(n,\gamma)$  cross sections of  $^{12}\text{C}$  [60] and  $^{16}\text{O}$  [61] have been successfully measured by resolving the represen-

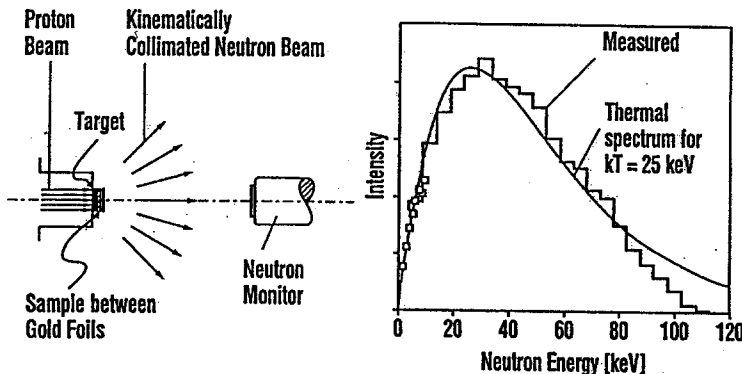


Fig. 9. The activation technique: irradiation of a sample sandwich at the accelerator (left) and the angle-integrated neutron spectrum (right).

tative  $\gamma$ -ray lines with a NaI detector.

**Activation measurements:** A completely different approach for the determination of stellar  $(n,\gamma)$  rates is by activation in a quasi-stellar neutron spectrum. Compared to the techniques based on the detection of prompt capture  $\gamma$ -rays, this method offers the advantages of superior sensitivity (which means that much smaller samples can be measured reliably - an important aspect for the investigation of radioactive isotopes on the *s*-process path), and of selectivity (which means that samples of natural composition can be studied instead of expensive enriched samples required by the TOF techniques). However, it is restricted to those cases, where neutron capture produces an unstable nucleus, and it yields the stellar rate only for two thermal energies at  $kT = 25$  and  $52$  keV. A proposal for obtaining spectra for other thermal energies [62] is presently investigated experimentally.

It is essential for this method that quasi-stellar neutron spectra can be produced in the laboratory via the  $^7\text{Li}(p,n)^7\text{Be}$  [63,64] and the  $^3\text{H}(p,n)^3\text{He}$  reactions [65]. In the first case, the proper neutron spectrum is obtained by bombarding thick metallic lithium targets with protons of 1912 keV, only 31 keV above the reaction threshold. The resulting neutrons exhibit a continuous energy distribution with a high-energy cutoff at  $E_n = 106$  keV and a maximum emission angle of 60 deg as shown in Fig. 9. The angle-integrated spectrum corresponds closely to a Maxwell-Boltzmann distribution for  $kT = 25$  keV. Hence, the reaction rate measured in such a spectrum yields immediately the proper stellar cross section. Irradiating the respective samples between two gold foils allows to use the  $^{197}\text{Au}(n,\gamma)$  cross section as a standard.

The activation technique has been applied in a variety of measurements, and was particularly important for the determination of partial cross sections leading to isomeric states [66,67]. Recent typical examples refer to the small cross

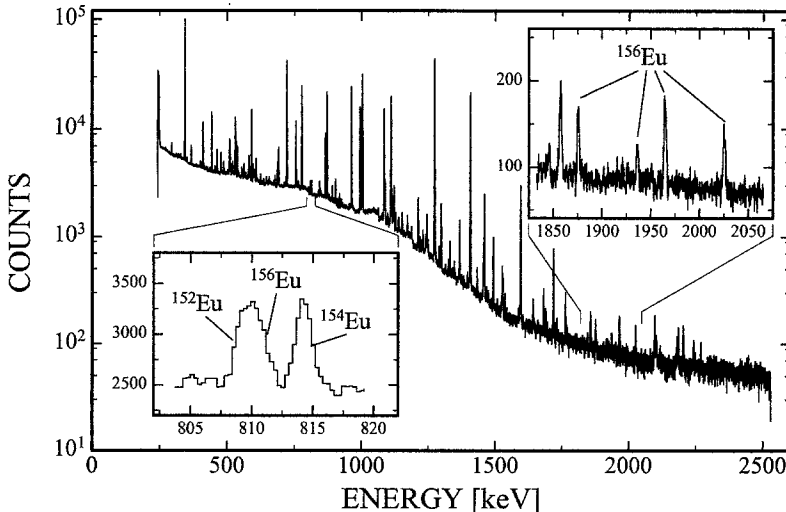


Fig. 10. The  $\gamma$ -ray spectrum after irradiation of a 88 ng  $^{155}\text{Eu}$  sample in a quasi-stellar neutron spectrum (from Ref.[72]).

sections of neutron magic isotopes [68] and light nuclei [69]. The technique is suited for reaction products with half-lives of several years down to a few msec [70] and allows for cross section measurements with uncertainties of a few %.

Another attractive feature of the activation technique is the possibility to investigate a number of unstable nuclei [71] of relevance for *s*-process branchings. An example of this category is  $^{155}\text{Eu}$  with a half-life of 4.96 yr which belongs to the branchings that are defined by the *s*-only isotopes  $^{152}\text{Gd}$  and  $^{154}\text{Gd}$ . Thanks to the high sensitivity of the activation technique, the sample activity could be minimized by using only 88 ng  $^{155}\text{Eu}$  corresponding to  $3.4 \times 10^{14}$  atoms for a successful cross section measurement. This sample was exposed for 17 days to the quasi-stellar spectrum obtained via the  $^7\text{Li}(\text{p},\text{n})^7\text{Be}$  reaction. After irradiation, the induced  $\gamma$ -activity was measured for 29 days with a HPGe detector. The resulting spectrum (Fig. 10) shows about 200 lines which originate mostly from a remaining Eu contamination of the sample. Nevertheless, 11 lines could be attributed to the decay of  $^{156}\text{Eu}$ , some being illustrated in the insets. From their intensities a stellar cross section of  $1490 \pm 90$  mb at 25 keV thermal energy was determined, five times more accurate than the best model calculations [72].

The available information on experimental  $(\text{n},\gamma)$  cross sections has been collected and converted to stellar values in a number of compilations [73–75].

#### 4.1.3 Other neutron cross sections

For a number of isotopes in the mass range  $A < 60$ , the  $(n,\alpha)$  and  $(n,p)$  cross sections become significant and may well exceed the neutron capture channel, thus leading to another type of  $s$ -process branchings. An important example is the  $^{14}\text{N}(n,p)^{14}\text{C}$  reaction [76,77], which represents a crucial neutron poison in low mass AGB stars. The cross section of the  $^{17}\text{O}(n,\alpha)^{14}\text{C}$  reaction plays a decisive role in inhomogeneous big bang models, since it hampers the synthesis of heavier elements [78,79].

The reactions  $^{33}\text{S}(n,\alpha)^{30}\text{Si}$  and  $^{36}\text{Cl}(n,p)^{36}\text{S}$  were intensively studied at stellar [80,81] and thermal [82] energies in order to understand whether the observed  $^{36}\text{S}$  abundance can be interpreted as a monitor for the  $s$ -process neutron exposure [80,83]. Similar measurements are required for a discussion of the  $^{40}\text{K}/^{40}\text{Ar}$  chronometer [84].

So far, very few measurements of elastic and inelastic scattering cross sections in the keV range have been performed in an astrophysical context. Pioneering work of this type [85–88] was carried out for a quantitative description of the stellar enhancement of the  $^{187}\text{Os}(n,\gamma)$  cross section, a critical point for interpreting the Re/Os chronometer (Sec. 6).

Finally, the neutron producing reactions during stellar helium burning deserve special attention. While the  $^{13}\text{C}(\alpha,n)^{16}\text{O}$  reaction dominates the neutron production in low mass AGB stars,  $^{22}\text{Ne}(\alpha,n)^{25}\text{Mg}$  is the main neutron source in massive stars. Though both reactions have been measured towards relatively low energies (see Refs.[89,90] and [89,91,92] for the  $^{13}\text{C}$  and  $^{22}\text{Ne}$  sources, respectively), there are still considerable uncertainties at the actual stellar energies. In view of their consequences for the stellar scenarios, these uncertainties should be reduced by additional measurements including complementary reaction channels and R-matrix analyses in order to account for possible interference effects of the involved resonances. The persisting difficulties with the  $^{22}\text{Ne}$  neutron source have been shown to refer to the yet unclear contribution from a resonance at 633 keV [93] suggested by  $\alpha$ -transfer experiments [94,95].

#### 4.1.4 Theoretical calculations

Despite of the experimental progress, cross section calculations for  $s$ -process studies are indispensable, (i) for determining the  $(n,\gamma)$  rates of branch point nuclei with high specific  $\gamma$ -activity, and (ii) for obtaining the (possible) differences between the laboratory values and the actual stellar cross sections. Naturally, theoretical calculations are much more important for explosive scenarios: the reaction paths are outside the stability valley, where experimental data are still completely missing. Insofar,  $s$ -process applications of calculated cross sections provide an important test for the quality of various theoretical

treatments.

With few exceptions, neutron capture rates between Fe and the actinides can be determined by means of the statistical Hauser-Feshbach approach [96–98]. The applicability of this model depends on the conditions that the level density in the compound nucleus must be high enough with at least  $\approx 10$  resonances contributing to the reaction rate, and that the energy of the incident particle be sufficiently low in order to ensure the compound nucleus picture to dominate. The second condition is practically always satisfied at *s*-process energies, because other reaction mechanisms require neutron energies of a few MeV. The first condition, however, is in question for all nuclei at or close to magic nucleon numbers, and must be considered individually [99]. In these cases, e.g. for  $^{208}\text{Pb}$ , the small contributions from direct capture mechanisms may already be significant [52].

The quality of the Hauser-Feshbach approach depends critically on the model parameters used. The first part of the calculation, the formation of the compound nucleus, is using the optical model. Information on the related parameters, which characterize the potential of the nucleus as felt by the incoming neutron (well depth, radius, absorptive properties) can be derived from a fit of total neutron cross sections, strength functions, and scattering radii. The more critical second step, the decay of the compound state through the photon channel, is commonly described with the Brink-Axel hypothesis that the dominant dipole transitions can be described through the cross section of the inverse reaction, namely through the extrapolated cross section of the giant dipole resonance. The most sensitive part for describing the photon decay is the level density in the compound nucleus. Experimental information on the level density comes from the known discrete levels from the ground state up to about 1 MeV and from high-resolution resonance studies at the neutron separation energy. In practical applications these data are used for parameterising a back-shifted Fermi gas formula.

**Local parameter sets:** Principally, two different philosophies were pursued in establishing parameter systematics for the statistical model. For applications to nuclei in or near the stability valley, *local* parameter sets were constructed from experimentally known quantities in rather limited mass regions [100–102]. In this way, the required parameters could be obtained preferentially by interpolation between similar nuclei. An example of this procedure is shown in Fig. 11 for the level density parameter  $a$  in the mass region  $145 < A < 155$  [103] that allowed to determine the respective values for the unstable branching points  $^{147}\text{Nd}$ ,  $^{147}\text{Pm}$ , and  $^{148}\text{Pm}$ . By sensitivity studies in several mass regions, calculations with this phenomenological procedure were shown to exhibit remaining uncertainties of typically 25%.

**Global parameter sets:** For nuclei far from stability, which are involved

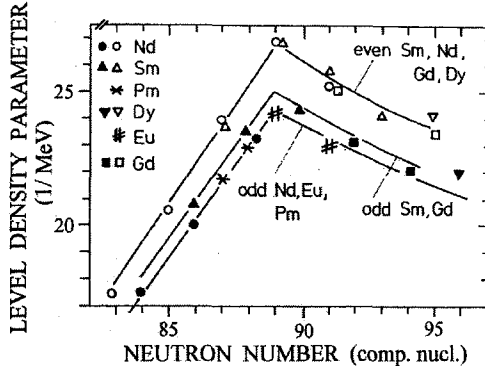


Fig. 11. *Local* systematics of the level density parameter  $a$  in the mass region  $145 < A < 155$  [103]. Open and full symbols represent the level densities for even and odd target isotopes as derived from experimental information. Interpolated values for  $^{147}\text{Pm}$  and  $^{148}\text{Pm}$  are indicated by stars.

in explosive scenarios, a different strategy has to be used for establishing a *global* parameter systematics. In this case, the corresponding prescriptions are formulated on theoretical grounds, including as many basic nuclear physics concepts as possible. Proton and neutron potentials based on microscopic infinite nuclear matter calculations for a given density and applied with a local density approximation and with corrections for the imaginary part were shown to reproduce the particle strength functions very well [17]. The  $\gamma$ -transmission coefficients for E2 transitions are derived from the Lorentzian representation of the giant dipole resonance and fit the resonance energy and width for stable nuclei [17]. The major difficulty in constructing these global parameter sets is the prediction of nuclear level densities. The presently favored solution is still based on the back-shifted Fermi-gas model [99], but includes an energy-dependent level density parameter and vanishing shell effects at high excitation energies [104,105]. This prescription yields level densities in good agreement with recent Monte Carlo shell model calculations [106].

Such a parameterization has been developed for the statistical model code SMOKER [107] with recent improvements for the new version NON-SMOKER [108]. If only the global parameter predictions for all input parameters are used without considering any experimental information, the calculated cross sections agree with the available measurements with an average deviation of about 40%. This is illustrated in Fig. 12 for the stellar  $(n, \gamma)$  cross sections. While the neutron capture rates as well as the proton capture rates [109,110] can be reproduced rather well, there are still problems with the  $\alpha$ -nucleus optical model potentials [111,112].

A similar update of the SMOKER code, the MOST version [113], includes

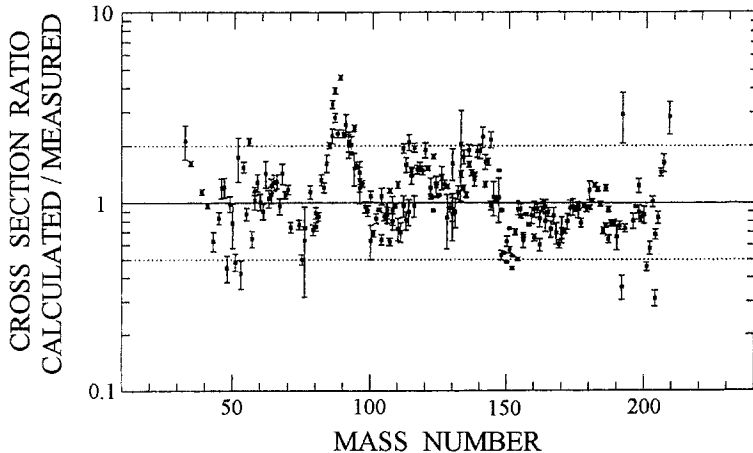


Fig. 12. Stellar  $(n,\gamma)$  cross sections calculated with the statistical model code NON-SMOKER are compared with the available experimental data [108].

also the direct capture part of the cross sections, which becomes significant for very neutron-rich nuclei towards the  $r$ -process path [114,115].

Comprehensive tables of calculated cross sections are meanwhile available [17,116,117] and widely used in a variety of astrophysical applications. Together with a number of related data, these tables and more recent updates are compiled by the LBNL Isotopes project and disseminated on the Nuclear Astrophysics homepage at <http://ie.lbl.gov/astro.html> [118].

#### 4.1.5 Stellar cross sections

In many cases, statistical model calculations have to be invoked for estimating the influence of temperature on the reaction rates. In the intense photon bath at the  $s$ -process site, low-lying nuclear levels can be significantly populated. Neutron captures in these states and the competition with new channels for downward inelastic scattering - the so-called *superelastic* scattering, where neutrons gain energy - may cause non-negligible differences between the laboratory cross section and the actual value in the stellar environment. This effect can be calculated by comparing the ground state cross section and the effective cross section for a thermally equilibrated nucleus, the ratio being denoted as the enhancement factor for the stellar cross section,  $SEF = \langle\sigma\rangle^{\text{star}} / \langle\sigma\rangle^{\text{lab}}$ .

These corrections are illustrated in Fig. 13 for the standard thermal energy of  $kT=30$  keV commonly used in  $s$ -process comparisons. About 25% of all isotopes involved in the  $s$  process show an effect of more than 2%, comparable to the uncertainty of a careful laboratory measurement (upper panel of Fig. 13). Significant corrections are to be expected for odd and/or deformed nuclei

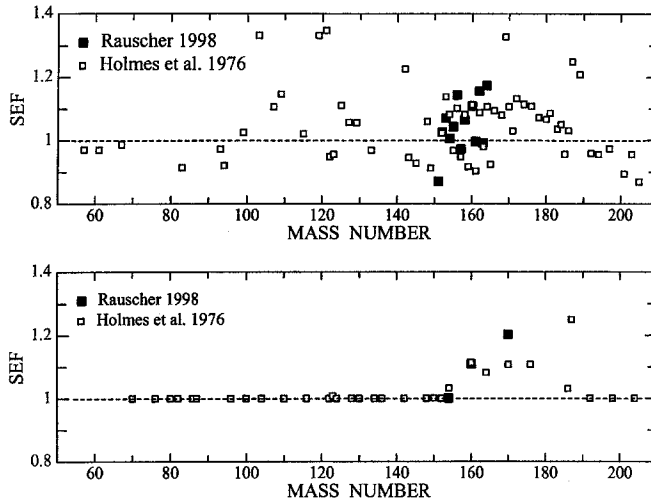


Fig. 13. Stellar enhancement factors for  $(n,\gamma)$  cross sections at 30 keV thermal energy. Top: All nuclei with corrections of more than 2%. Bottom: Enhancement factors for the important *s*-only isotopes. Data are from Ref.[116] (open symbols) and from Ref.[119] (black squares).

with excited states well below 100 keV. Correspondingly, the ensemble of *s*-only isotopes is little affected, except for the mass region  $160 < A < 190$  (lower panel of Fig. 13).

The only cases, where this correction has been carefully investigated, are the  $^{187}\text{Os}$  and  $^{191}\text{Os}$  cross sections [85–88,120], which are important for the Re/Os chronometer (Sec. 6). In view of the importance of this effect, at least the critical *s*-only isotopes should also be studied in detail, including complementary measurements of the elastic and inelastic cross sections. This broader data basis would then allow to understand whether the cross section enhancements calculated with the statistical model are sufficiently reliable.

#### 4.1.6 Status and perspectives

In Fig. 14, the stellar  $(n,\gamma)$  rates of the even-even nuclei between Fe and Pb are plotted to illustrate the current improvements of this data base, indicated by the small uncertainties on many of the data points, even in the deep minima at magic neutron numbers. A large number of new measurements helped also to resolve discrepancies between previous data. More and better cross sections are still needed, particularly in the region from Mo to Pd, where large uncertainties exist. In some cases, experimental data are yet completely missing, i.e. for isotopes of Ge and Se as well as for the important *s*-only nuclei  $^{128}\text{Xe}$ ,  $^{130}\text{Xe}$ , and  $^{192}\text{Pt}$ .

In general, Maxwellian averaging for the "standard" thermal energy of  $kT$

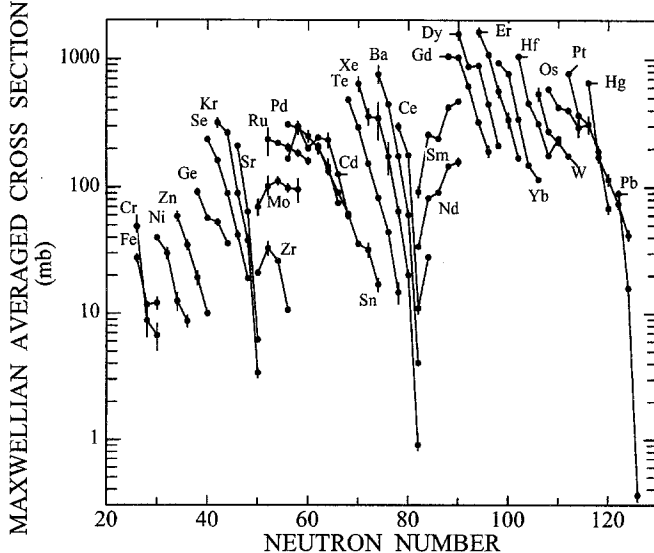


Fig. 14. Status of stellar  $(n,\gamma)$  cross sections for a thermal energy of  $kT=30$  keV, illustrated at the example of the even-even nuclei between Fe and Pb. Note the deep minima in this distribution at magic neutron numbers.

$= 30$  keV requires data in the energy range from a few keV up to  $\sim 200$  keV. Stellar models suggest, however, that the  $s$  process may partly operate at much lower temperatures corresponding to  $kT=8$  keV, which means that stellar cross sections are also sensitive to contributions from lower energies as in the case of  $^{138}\text{Ba}$  [52]. In this respect, it can be important to combine data obtained in different energy regions using different techniques at different facilities.

This is illustrated by the struggle for a consistent set of stellar  $(n,\gamma)$  cross sections of the barium isotopes. Due to the nearby magic neutron number 82, these cross sections are small and, therefore, difficult to measure. Significant discrepancies among recent measurements [51,121,122] originated partly from the fact that the first experiment with the Karlsruhe  $4\pi$   $\text{BaF}_2$  detector was hampered by background from scattered neutrons which were captured in the barium nuclei of the scintillator. Therefore, the data could be analyzed only above 5 keV neutron energy, and a significantly larger overall uncertainty of 3% had to be considered compared to the typical 1% uncertainty claimed for this setup [123]. Furthermore, the missing information at low energies had to be adopted from the previously reported resonance data. While this correction had little influence at the higher thermal energy of 30 keV, it caused a large additional uncertainty in the 10 keV values [121].

When the high-resolution data of Ref. [51] became available, they were in excellent agreement at  $kT=30$  keV, but the 10 keV values differed by more than the quoted uncertainties. This discrepancy disappeared when the new resonance parameters of Ref. [51] were used to complement the data set of

Table 1

The stellar cross sections for  $^{134}\text{Ba}$ ,  $^{136}\text{Ba}$ , and  $^{137}\text{Ba}$ 

Experiment	kT <sup>a</sup> =	Stellar ( $n,\gamma$ ) cross section (mbarn)		
		$^{134}\text{Ba}$	$^{136}\text{Ba}$	$^{137}\text{Ba}$
Karlsruhe VdG	kT=30	173.6±5.6	61.2±2.0	76.9±3.3
$4\pi \text{ BaF}_2$ , 1995 [121] <sup>b</sup>	10	289.5±10.5	115.6±4.4	137.7±10.6
Oak Ridge LINAC	kT=30	179.0±5.7	62.0±2.0	75.7±2.4
PH weighting, 1996/98 [51,124]	10	276.0±8.8	122.0±3.9	142.2±4.4
Geel LINAC	kT=30	.....	60.4±2.9	.....
PH weighting, 1997 [122]	10	.....	108.6±4.0	.....

<sup>a</sup>Complemented with resonance data of Ref. [51] below 5 keV<sup>b</sup>Thermal energy in keV

Ref. [121] at very low energies. The resulting agreement is summarized in Table 1 and was further supported by independent experiments on  $^{136}\text{Ba}$  [122] and  $^{137}\text{Ba}$  [124]. This example illustrates that different techniques are, indeed, producing consistent data within the quoted uncertainties, and that the overall quality can be improved by combining complementary methods.

According to the range of thermal energies from  $\approx 8$  keV in low mass stars up to 80 keV during carbon burning in massive stars, the relevant neutron energy range extends up to a few hundred keV. A satisfactory data base for *s*-process studies should, therefore, contain experimental information over a sufficiently wide energy range, and with uncertainties of about 5 %. Beside these general requirements, data with typical uncertainties of 1% are needed for the *s*-only nuclei, which are important as normalization points for the *s*-abundance distribution and for defining the *s*-process branchings as well as for the interpretation of isotopic anomalies in meteoritic inclusions.

The cross sections for neutron-magic nuclei and for the abundant light isotopes, which represent the major neutron poisons, should be known to better than 5 % despite of the persisting difficulties in the investigation of these small cross sections. The importance of these isotopes is illustrated by the examples of  $^{138}\text{Ba}$  [52] and  $^{142}\text{Nd}$  [125], where accurate cross section data led to strong constraints for *s*-process models (Sec. 4.3). For the majority of isotopes in this group, the requested accuracy is still far from being satisfied.

Further improvements are definitely needed for the ( $n,\gamma$ ) cross sections of radioactive targets. Such measurements are hampered by the background from

the sample activity, but also because suited samples are not easily available.

The discussion of experimental possibilities for measurements on short-lived branch-point nuclei showed [126] that a number of these cases can be studied with samples of a few mg using optimized TOF techniques at electrostatic accelerators or using the much higher flux at spallation sources. In this context, the activation technique was found to be a particularly suited option for ( $n,\gamma$ ) measurements on unstable nuclei [126] since it allows to reduce the required sample mass by another factor of 10,000. A correspondingly small sample was successfully used for measuring the cross section of the radioactive branch-point nucleus  $^{155}\text{Eu}$  ( $t_{1/2}=4.96\text{ yr}$ ) [72].

Since very small samples are sufficient, such studies could benefit from future radioactive ion beam facilities: intensities of  $10^9 \text{ s}^{-1}$  allow to produce appropriate samples within a few hours, presumably with considerably better purity than can be achieved by radiochemical methods.

#### 4.1.7 Beta-decay rates

Isotopes, which are exposed to high temperatures and densities in a stellar plasma, may experience a dramatic enhancement of their decay rate. This idea was formulated by Cameron [127] and was detailed soon later [128,129]. As nuclear matrix elements remain unchanged, the stellar decay rates can be calculated from pure phase space arguments, at least for the relevant allowed and first non-unique forbidden transitions [128].

The enhancement results from different effects related to the thermal population of excited nuclear states in the hot photon bath or through atomic effects in the highly ionised, dense stellar plasma.

In thermal equilibrium, the population probability is determined by the Boltzmann factor and the statistical weight,

$$p_i = \frac{(2J_i + 1) \times \exp(-E_i/kT)}{\sum_m (2J_m + 1) \times \exp(-E_m/kT)},$$

the sum in the denominator being the nuclear partition function. Therefore, the actual stellar decay rate

$$\lambda_\beta^* = \sum_i \left( p_i \times \sum_j \lambda_{\beta ij} \right),$$

includes the decays of all thermally populated excited states  $i$  into the accessible levels  $j$  of the daughter nucleus. At 30 keV thermal energy, nuclear states at 100 keV excitation energy are typically populated with 1% probability. If

such a state decays 1000 times faster than the ground state, this implies in first approximation a stellar enhancement by a factor 10.

At He burning temperatures,  $\beta$ -decay rates can also be influenced by the almost complete ionization of the atoms. Under these conditions, electrons can be emitted into unoccupied atomic orbits, thus adding the respective binding energy to the decay energy of the neutral atom. This bound state  $\beta$ -decay is always important when the decay energy is comparable to or smaller than the K-shell binding energy. Bound state decay can even lead to the amazing result that terrestrially stable isotopes become unstable under *s*-process conditions if the isobaric mass difference is sufficiently small.

Naturally, electron capture (EC) decay is severely hampered for ionized atoms. For example, above an energy of 25 MeV/nucleon  $^7\text{Be}$  cannot capture an electron and behaves as if it were stable. Due to the high electron density of the stellar interior, this effect is balanced due to electron captures from the continuum, thus adding the pressure to the parameters that can influence the decay rate. Another consequence of the high electron density is the reduction and increase of the phase space for  $\beta^-$ - and  $\beta^+$ -decays, respectively.

These effects have been considered in a comprehensive tabulation of the relevant stellar decay rates along the *s*-process path by Takahashi and Yokoi [130]. This work provided the necessary basis for quantitative analyses of those *s*-process branchings, where the  $\beta$ -decay of the branch point depends on temperature and density.

Fig. 15 shows the ratios of the stellar decay rates and the terrestrial rates, for the most important branch point nuclei. Obviously, these enhancement factors for  $\beta$ -decay fall into two groups, one showing almost no enhancement at the reference temperature corresponding to 30 keV thermal energy, and a second one suffering a pronounced acceleration of the decay. Accordingly, the abundance patterns of the first type of branchings is suited for the determination of the *s*-process neutron density while the second group can be interpreted in terms of the *s*-process temperature. The enhancement factors differing by large factors provides an additional test for the consistency of the branching analyses and, hence, for the investigated model.

**Experimental possibilities:** Thermal enhancement effects are difficult to study in the laboratory since in practically all cases excited nuclear states decay much faster via  $\gamma$ -emission than by  $\beta$ -decay. The only example, where the  $\beta$ -decay half-life of an excited state was successfully measured, was carried out on  $^{79}\text{Se}$ . In this isotope, the enhancement is determined by the  $\beta$ -decay branch from the 96 keV isomer ( $t_{1/2}=4\text{ min}$ ), which could be detected in a reactor experiment [131].

Alternatively, charge exchange reactions have been used to determine  $\beta$ -decay

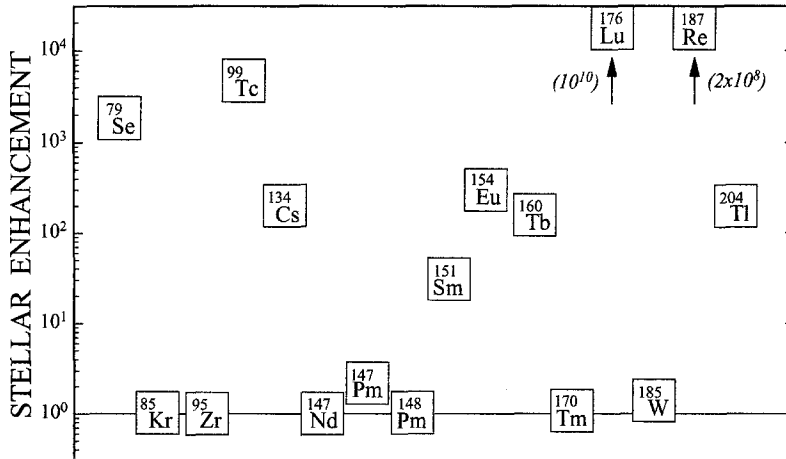


Fig. 15. The stellar enhancement of the decay (stellar decay rate/terrestrial rate) for some important branch point nuclei on the *s*-process path at  $kT=30$  keV. (Data are from Ref.[130]).

matrix elements [132]. These experiments are based on the proportionality between the forward-angle differential cross sections and the reduced nuclear matrix elements [133,134]. Originally, ( $p,n$ ) reactions at beam energies above 100 MeV were investigated, but more recently ( ${}^3He,t$ ) reactions were found to be of advantage because these can be studied with magnetic spectrometers that combine superior energy resolution, high projectile efficiency, and large solid angle [135]. This technique is also suited for studies with radioactive ion beams in inverse kinematics, e.g. via ( ${}^6He,{}^6Li$ ) reactions.

Another indirect determination of a stellar  $\beta$ -decay life time was carried out for  ${}^{176}\text{Lu}$  where thermal excitation of the short-lived,  $\beta$ -unstable isomer was quantified in a detailed study of the level scheme by means of several reactions. In this case, it was shown that the half-life of the potential *s*-process chronometer  ${}^{176}\text{Lu}$  ( $t_{1/2}=36$  Gyr) reduces to a few years at the temperatures of the He burning zones. Accordingly, the observed  ${}^{176}\text{Lu}$  abundance can be interpreted as thermometer for the *s*-process site [136,137].

The possibility to accelerate and to store relativistic heavy ions at GSI Darmstadt allowed to verify the mechanism of bound state  $\beta$ -decay at the examples of  ${}^{163}\text{Dy}$  and  ${}^{187}\text{Re}$ . If these terrestrially stable isotopes are completely stripped of their electrons, the electron binding energy adds to their marginally negative  $Q_\beta$  values, thus enabling the emission of electrons into the unoccupied orbits. In the GSI measurements, stripped ions were accumulated in the storage ring and their decay followed over a period of several hours. In this way, the half-lives for bound state decay could be measured for  ${}^{163}\text{Dy}$  [138] and  ${}^{187}\text{Re}$  [139,140], and were found in good agreement with the calculated values [130]. In all other cases, the stellar enhancement was calculated by using  $\beta$ -decay

matrix elements for the excited states that were derived via the systematics of known analogous transitions. A detailed discussion of the related problems and uncertainties is given in Ref.[130].

In principle, the very high  $\gamma$ -intensities achieved at synchrotron facilities, for example at the ESRF in Grenoble, could allow for sufficiently sensitive activation measurements to find the weak  $\beta$ -decay branch of short-lived excited states. The possibility to identify even a few  $\beta$ -decay products in storage ring experiments at GSI may provide an alternative approach for this challenging experimental problem.

## 4.2 The canonical $s$ process

### 4.2.1 The $\sigma N$ -curve

This phenomenological  $s$ -process picture was sketched already by B<sup>2</sup>FH and was later improved mainly by Seeger et al. [141]. In this approach it is empirically assumed that a certain fraction  $G$  of the observed  $^{56}\text{Fe}$  abundance was irradiated by an exponential distribution of neutron exposures

$$\rho(\tau) = \frac{G \times N_{56}^{\odot}}{\tau_0} \times \exp(-\tau/\tau_0).$$

In this case, an analytical solution can be obtained for the system of coupled differential equations describing the abundance changes along the reaction path from Fe to Bi

$$\frac{dN_s(A)}{dt} = \lambda_n(A-1)N_s(A-1) - (\lambda_n(A) + \lambda_\beta(A))N_s(A),$$

provided that a possible time dependence of the neutron capture rates,  $\lambda_n = n_n \langle \sigma \rangle v_T$  is neglected. In other words, it is assumed that temperature and neutron density,  $n_n$ , are constant. Then, the product of stellar cross section and resulting  $s$  abundance, which is the characteristic  $s$ -process quantity, can be given in analytic form,

$$\langle \sigma \rangle_{(A)} N_{s(A)} = \frac{G \cdot N_{56}^{\odot}}{\tau_0} \prod_{i=56}^A \left(1 + \frac{1}{\tau_0 \langle \sigma \rangle_i}\right)^{-1}.$$

Apart from the two parameters  $G$  and  $\tau_0$  (which are adjusted by fitting the abundances of the  $s$ -only nuclei), the remaining input for this expression are the stellar ( $n, \gamma$ ) cross sections  $\langle \sigma \rangle$ . Further details may be found in Ref.[13].

Given the very schematic nature of this classical approach, it was surprising to see that it provides an excellent description of the  $s$ -process abundances. Fig.

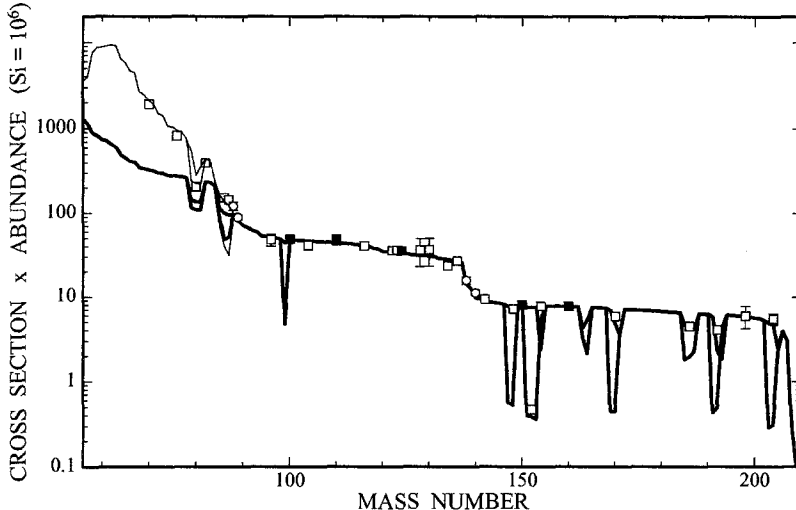


Fig. 16. The characteristic product of cross section times *s*-process abundance plotted as a function of mass number. The solid line was obtained via the classical model, and the symbols denote the empirical products for the *s*-only nuclei. A complete representation of the empirical products requires at least two different processes, the **main** and **weak** components indicated by thick and thin solid lines, respectively. Some important branchings of the neutron capture chain are indicated as well.

16 shows the calculated  $\langle\sigma\rangle N_s$  values compared to the corresponding empirical products of the *s*-only nuclei (symbols) in the mass region between  $A = 56$  and 209. The error bars of the empirical points reflect the uncertainties of the abundances and of the respective cross sections. One finds that equilibrium in the neutron capture flow was reached between magic neutron numbers, where the  $\langle\sigma\rangle N_s$ -curve is almost constant. The small cross sections of the neutron magic nuclei around  $A \sim 88$ , 140, and 208 act as bottlenecks for the capture flow, resulting in the distinct steps of the  $\sigma N$ -curve.

The global parameters,  $G$  and  $\tau_0$ , that determine the overall shape of the  $\langle\sigma\rangle N_s$ -curve, represent a first constraint for the stellar *s*-process site with respect to the required seed abundance and total neutron exposure. It is found that 0.04% of the observed  $^{56}\text{Fe}$  abundance are a sufficient seed, and that on average about 15 neutrons are captured by each seed nucleus [142]. These numbers refer to the **main** *s*-process component given by the thick line in Fig. 16. For  $A < 90$ , this line falls below the empirical points, thus requiring an additional **weak** component (thin line). The excellent agreement between the empirical points and the data obtained with the classical model is quite remarkable. In fact, those *s*-only nuclei that are not affected by branchings, are reproduced by the model with a mean square deviation of 3% [142].

The only mass region, where the two-component form of the *s* process was found to yield no satisfactory description was the termination point in the

Pb/Bi isotopes. These are the last stable nuclei before the reaction path hits the region of  $\alpha$ -instability, where the *s*-process flow is finally halted. In particular, only one third of the abundance of the doubly magic nucleus  $^{208}\text{Pb}$  could be produced in this way. Since also the trans-bismuth *r* contributions are likely to be small compared to the observed abundance, an additional *s* component was proposed [143]. This **strong** component was supposed to have a sufficiently large neutron exposure allowing for about 100 neutron captures per iron seed to drive a very small fraction of seed nuclei to a near-equilibrium recycling distribution in the mass region between  $^{206}\text{Pb}$  and  $^{209}\text{Bi}$ . Such a distribution favors mainly the production of the missing  $^{208}\text{Pb}$  because of its very small cross section.

In terms of stellar sites, the **main** component can be attributed to helium shell burning in low mass stars, where neutron production and concordant *s*-processing occur in two steps, by the  $^{13}\text{C}(\alpha,\text{n})^{16}\text{O}$  reaction at relatively low temperatures of  $T_8 \sim 1$  (where  $T_8$  denotes the temperature in units of  $10^8$  K) and by the  $^{22}\text{Ne}(\alpha,\text{n})^{25}\text{Mg}$  reaction at  $T_8 \sim 3$  (Sec. 4.3.1).

As a consequence of the comparably short time scales suggested by this model and the strong impact of convection, the *s* process in red giants differs completely from the assumption of a steady situation made in the classical approach. In order to account for the more complex stellar scenario, the canonical model was recently complemented by a network code [144] and by a parameterized model [52] for describing the combined action of the pulsed  $^{13}\text{C}$  and  $^{22}\text{Ne}$  sources. A different approach has been suggested by Goriely [145] representing the *s*-abundance distribution with a multi-event model, where a superposition of canonical events characterized by a wide range of temperatures and neutron densities is assumed without hypothesizing about a certain form of the exposure distribution [145,146] (see also Sec.4.3).

The **weak** component has been ascribed to core helium burning and more advanced stages in massive stars [147–150] when the temperatures become sufficiently high for neutron production via the  $^{22}\text{Ne}(\alpha,\text{n})^{25}\text{Mg}$  reaction. In these stars, the contribution from core helium burning dominates the *s*-process yields. During this phase, the neutron density is comparably low and lasts for about  $3 \cdot 10^4$  yr, resulting in the modest neutron exposure of the weak *s*-process component.

The models for the scenarios suggested for the main and weak components can best be tested by detailed analyses of the *s*-process branchings that occur in the respective mass regions.

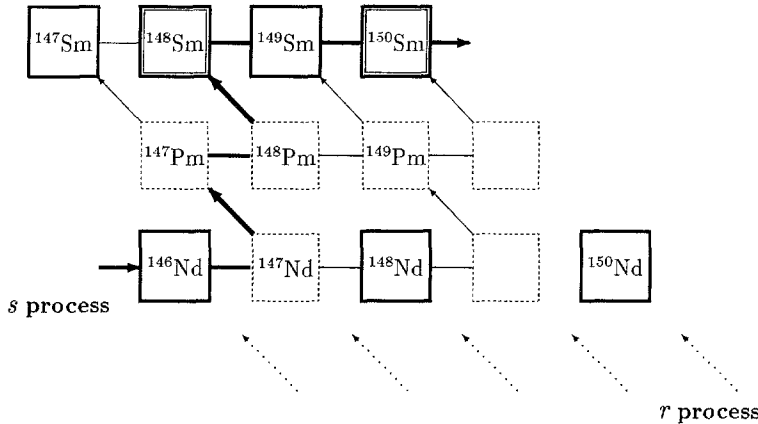


Fig. 17. The *s*-process reaction path in the Nd/Pm/Sm region with the branchings at A=147, 148, and 149. Note that  $^{148}\text{Sm}$  and  $^{150}\text{Sm}$  are shielded against the *r* process. These two isotopes define the strength of the branching.

#### 4.2.2 Branchings in the *s*-process path

A branching in the reaction flow occurs when an unstable nucleus is encountered which exhibits comparable neutron capture and  $\beta$ -decay rates. The resulting abundance pattern can be used to determine information on the physical conditions during the *s* process. The example of Fig. 17 shows the *s*-process flow in the mass region between neodymium and samarium, with the possible branchings at  $^{147}\text{Nd}$  and  $^{147-149}\text{Pm}$ . Note that  $^{148}\text{Sm}$  and  $^{150}\text{Sm}$  are shielded against the *r* process by their isobars in neodymium. As the result of a significant branching at A = 147 - 149, the  $\langle\sigma\rangle N_s$  value of  $^{150}\text{Sm}$  will, therefore, be larger than that of  $^{148}\text{Sm}$ .

The strength of a branching can be expressed in terms of the rates for  $\beta$ -decay and neutron capture of the involved branch point nuclei as well as by the  $\langle\sigma\rangle N_s$  values of the involved *s*-only isotopes,

$$f_\beta = \frac{\lambda_\beta}{\lambda_\beta + \lambda_n} \approx \frac{(\langle\sigma\rangle N_s)_{^{148}\text{Sm}}}{(\langle\sigma\rangle N_s)_{^{150}\text{Sm}}} \approx 0.9.$$

Inserting the equations for the decay rates this expression can be solved for the neutron density. If - for simplicity - only the branching at  $^{148}\text{Pm}$  is considered, one obtains

$$n_n = \frac{1 - f_\beta}{f_\beta} \cdot \frac{1}{v_T \langle\sigma\rangle_{^{148}\text{Pm}}} \cdot \frac{\ln 2}{t_{1/2}^{*}(^{148}\text{Pm})}.$$

This equation illustrates the input data that are important for reliable branching analyses.

- The first term depends on the cross sections for the *s*-only nuclei, which define the branching factor  $f_\beta$ . Since the neutron density is required to

$\sim 10\%$ , the branching factor, and, hence, the cross sections for the *s*-only nuclei need to be known to about 1% in many cases. While conventional techniques are limited to uncertainties  $> 4\%$ , the required accuracy can be obtained with the  $4\pi$  BaF<sub>2</sub> detector.

- The second term contains the stellar cross sections of the radioactive branch point isotopes. Since practically no measurements exist for the unstable branch point nuclei, only calculated cross sections are available at present. But even the most careful statistical model calculations are limited to uncertainties of 20% to 30%, not sufficient for deducing the entire information contained in the abundance patterns. For some of these short-lived nuclei, experimental cross section studies aiming at a 5% to 10% uncertainty were recently suggested [72,126].
- The last term denotes the stellar decay rate of the branch point isotope. While there is no difference between the stellar and the terrestrial rate for some of the branch points, a variety of examples exhibit sometimes drastic changes under the high temperatures and densities of the stellar plasma.

Since the  $\beta$ -decay rates of the branch points at A=147-149 in Fig. 17 are not significantly affected by temperature (see Fig. 15), these branchings can be used for a determination of the *s*-process neutron density. Compared to the previous result [103] ( $f_\beta = 0.92 \pm 0.04$ ), the measurement with the  $4\pi$  BaF<sub>2</sub> detector yields  $f_\beta = 0.870 \pm 0.009$ , with a 4 times smaller uncertainty [123]. Compared to the previous estimate of  $n_n = (3.4 \pm 1.1) \cdot 10^8 \text{ cm}^{-3}$  [142], the revised branching factor implies a considerably improved neutron density of  $(4.1 \pm 0.6) \cdot 10^8 \text{ cm}^{-3}$  [68].

There are about 15 to 20 significant branchings along the *s*-process path, which can be studied with respect to the physical conditions at the stellar site. In a first step, the neutron density must be obtained from those branchings which are not affected by temperature. With this information, the branching factors of the remaining cases can be derived and the mean stellar decay rates be determined. Eventually, the dependence of these rates on temperature and/or electron density yields the *s*-process temperature and mass density [142]. The present status of branching analyses with the classical approach is summarized in Table 2. Prominent examples in this list are from the lanthanide region, which is particularly important in this context because the chemical similarity of these elements implies that their relative abundances are well defined. Therefore, the total reaction flow can be normalized at the unbranched *s*-only isotope <sup>150</sup>Sm, analogously to the situation of Fig. 17. The lanthanide branchings occur at A=141, 151, 154, 163, 169, and 176 and are defined by the *s*-isotopes <sup>142</sup>Nd, <sup>152</sup>Gd, <sup>154</sup>Gd, <sup>164</sup>Er, <sup>170</sup>Tm, and <sup>176</sup>Lu, respectively.

As far as the neutron density is concerned, the best value,  $n_n = (4.1 \pm 0.6) \cdot 10^8 \text{ cm}^{-3}$ , is in good agreement with the estimate obtained from the <sup>185</sup>W/<sup>186</sup>Re branching. The various estimates of the *s*-process temperature are also com-

Table 2

Results from various branching analyses of relevance for the main *s*-process component

Branch point isotope	Deduced <i>s</i> -process parameter	Reference
$^{147}\text{Nd}/^{147}\text{Pm}/^{148}\text{Pm}$	$n_n = (4.1 \pm 0.6) \cdot 10^8 \text{ cm}^{-3}$	[123]
$^{151}\text{Sm}/^{154}\text{Eu}$	$T_8 = 3.5 \pm 0.4$	[58]
$^{163}\text{Dy}/^{163}\text{Ho}$	$\rho_s = (6.5 \pm 3.5) \cdot 10^3 \text{ g cm}^{-3}$	[151]
$^{176}\text{Lu}$	$T_8 = 3.1 \pm 0.6$	[137,152]
$^{121}\text{Sn}/^{122}\text{Sb}$	$T_8 > 2.4$	[153]
$^{134}\text{Cs}$	$T_8 = 1.9 \pm 0.3$	[154]
	$T_8 = 1.7 \pm 0.5$	[51]
$^{185}\text{W}/^{186}\text{Re}$	$n_n = (3.5^{+1.7}_{-1.1}) \cdot 10^8 \text{ cm}^{-3}$	[155]

$$kT = 8.62 \times T_8 \text{ keV}$$

patible with each other, except for the result from the  $^{134}\text{Cs}$  branching. This discrepancy, however, may originate from an uncertainty in the temperature-dependent decay rate of  $^{134}\text{Cs}$  which had been noted explicitly [130]. Hence this problem should be investigated further before the  $^{134}\text{Cs}$  branching can be discussed in any quantitative way.

The currently best estimates for the temperature have been derived from the branchings at  $^{151}\text{Sm}/^{154}\text{Eu}$  [58] and at  $^{176}\text{Lu}$  [137,152], which constrain the *s* process temperatures in different ways. The half-lives of the branch points  $^{151}\text{Sm}$  and  $^{154}\text{Eu}$  decreasing steadily with increasing temperature implies that these branchings are still sensitive to the neutron density. According to the stellar models (Sec. 4.3), the neutron density exhibits strong fluctuations and depends also on the neutron source reactions. In contrast,  $^{176}\text{Lu}$  exhibits a very different temperature-dependence, which is related to its complicated nuclear structure. Though the enhancement of the decay rate is due to the short-lived isomer at 123 keV excitation energy, this state cannot directly be populated in the usual way by thermally induced transitions from the ground state. Because transitions from the ground state are highly forbidden by selection rules, the isomer can only be reached via gateway levels, which occur at excitation energies of 838 keV and above [136,137,156]. Since these levels are populated at rather high temperatures, the  $^{176}\text{Lu}$  decay is accelerated above about  $T_8=2$ . Hence, the lower limit of  $T_8=2.5$  obtained via this thermometer [152] represents a firm constraint for the *s*-process temperature.

The fact that this limit is higher than the ignition temperature of the  $^{13}\text{C}$  neutron source bears the important consequence that the  $^{176}\text{Lu}$  branching must

have been determined by the  $^{22}\text{Ne}$  source. Therefore, it reflects the relative contributions of the two sources to the total neutron exposure [152].

A first attempt to determine the mass density in the *s* process was carried out by Beer, Walter, and Macklin [157] by analyzing the small branching to  $^{164}\text{Er}$ . Their value,  $\rho_s = (8 \pm 5) \cdot 10^3 \text{ g cm}^{-3}$ , is in reasonable agreement with the recent analysis cited in Table 2 [151].

So far, the results from the different branchings are still consistent with each other. This means that they still satisfy the assumption of the classical approach that neutron density and temperature are constant during the *s* process. In contrast, stellar models suggest these parameters to vary strongly with time. Consequently, the freeze-out at the end of each neutron exposure may well cause a distortion of the abundance pattern predicted by the classical approach. Since these effects are still obscured by the present uncertainties of the input data, future efforts have to concentrate on improving the relevant cross sections and  $\beta$ -decay rates for all of the important *s*-process branchings in order to achieve a more detailed picture.

#### *4.2.3 Limits of the canonical approach*

Though the canonical model was based on oversimplified assumptions concerning the He burning scenarios, it was surprisingly successful in describing the *s*-process abundance distribution as well as the *s*-process branchings [142]. With the availability of improved  $(n, \gamma)$  cross sections, however, the limitations of this approach became apparent. Unexpectedly, first hints for an inconsistency resulted not from branching analyses but from problems in reproducing the overall abundance distribution, when significant overproductions of the *s*-only isotopes  $^{136}\text{Ba}$  and  $^{116}\text{Sn}$  were observed as a consequence of accurate Ba [154] and Sn [158] cross section measurements.

While these failures were still masked by the relatively large uncertainties of the solar Ba and Sn abundances [26], firm evidence for a notorious inconsistency of the canonical model came from an experiment on a series of Nd isotopes [125,159]. The improved data showed that the *s*-only nucleus  $^{142}\text{Nd}$  was overproduced by 12%, corresponding to a significance of more than five standard deviations. This result implies *s*-process neutron exposures, which must be very different from the exponential distribution assumed for the canonical approach.

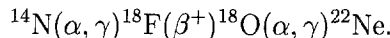
Therefore, this model can no longer be used in the vicinity of closed neutron shells, where the small cross sections did not allow to establish reaction flow equilibrium. In mass regions between magic numbers, the local approximation may still be a useful tool for determining the *s* abundances as long as these are not affected by branchings.

### 4.3 Stellar *s*-process models

During most of their life, stars are quietly burning their central hydrogen inventory. The stellar structure during that phase is characterized by the equilibrium between the gravitational pressure exerted by the outer layers and the radiation pressure created by the energy production in the interior, a situation that can be described, for example, by the standard solar model [160]. After hydrogen exhaustion in the central region, stellar evolution speeds up and becomes much more violent. While hydrogen burning continues in a shell around the center, the inert helium core is no longer producing the energy to maintain the radiation pressure. Therefore, it shrinks and heats up by the released gravitational energy until He burning is ignited at temperatures in excess of  $T_8 \sim 1.5$ . The high central temperatures cause the stars to expand and to cool on the outside - they are becoming red giants.

The convincing observational evidence for red giants as the astronomical site of the *s* process was first complemented by stellar models developed by Weigert [161] and Schwarzschild and Härm [162], who showed that stars with masses  $M < 9M_\odot$  develop a convective He burning shell during their AGB stage of evolution. Since this He shell burned via repeated He flashes in partially overlapping mass zones, this picture was intimately linked to the canonical model. As shown by Ulrich [163] this overlap led quite naturally to the exponential neutron exposure,  $\rho(\tau)$ , which had been obtained empirically by the canonical model [141].

The pulsating He shell model was further developed in a series of papers by Iben and collaborators [164–168]. This scenario was first explored for intermediate mass stars in the range  $4 < M_\odot < 8$  with the  $^{22}\text{Ne}(\alpha, n)$  reaction as the dominant neutron source, the  $^{22}\text{Ne}$  being produced from the ashes of the CNO cycle via the reaction sequence



Tests of the concordant *s*-process synthesis showed, however, that the predicted neutron densities and temperatures were far too high for reproducing the abundance patterns of the branchings [169]. Furthermore, no evidence for an enhancement of  $^{25}\text{Mg}$  was found in spectroscopic observations of MgH bands in S stars, which typically exhibit strong *s*-process enhancements, thus excluding the  $^{22}\text{Ne}(\alpha, n)^{25}\text{Mg}$  reaction as the major neutron source [42,170].

Subsequently, the interest was focused on low mass stars between 1 and  $3 M_\odot$  [171] where neutrons are mainly produced via the  $^{13}\text{C}(\alpha, n)^{16}\text{O}$  reaction already at significantly lower temperatures of  $T_8 = 1$  to 1.5. This *s*-process site turned out to be consistent with the observed *s* enhancements [172,173] and with the observation that the *s* abundances in unevolved stars are correlated with

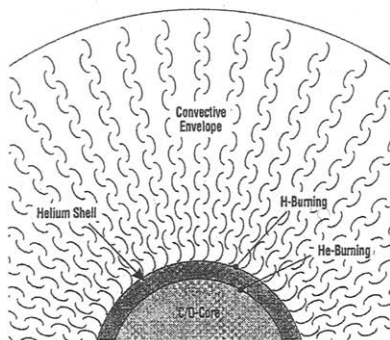


Fig. 18. The structure of a  $3M_{\odot}$  star during its He shell burning phase on the AGB. The extension of the core and the He shell are not to scale (see Fig. 19).

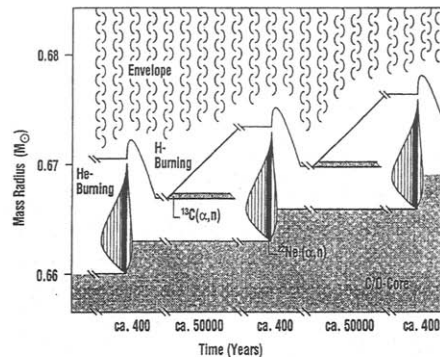


Fig. 19. The evolution scheme during the He shell burning phase. Note the different H and He burning time scales and the growing C/O core. Neutrons are produced by  $(\alpha, n)$  reactions on  $^{12}\text{C}$  and  $^{22}\text{Ne}$  during H and He burning, respectively.

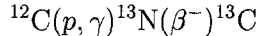
the respective iron abundances [32]. This *primary* nature indicates that the *s* process efficiency is roughly independent of the metallicity, quite different from the neutron supply based on  $^{22}\text{Ne}$ , which is produced from the initial CNO abundances. (Metallicity denotes the sum of all elemental abundances relative to hydrogen and helium.; the metallicity of the Sun is  $Z = 0.02$ ).

#### 4.3.1 Helium Shell Burning in Low mass AGB stars

The stellar structure in this stage of evolution is sketched in Figs. 18 and 19. Energy is produced in a narrow double shell on top of an inert core consisting of  $^{12}\text{C}$  and  $^{16}\text{O}$  as sketched in Fig. 19, where the mass radius of the  $3 M_{\odot}$  star chosen for this example is plotted against evolution time. The inert C/O core has already grown to  $0.66 M_{\odot}$  while the energy producing layer is confined within  $10^{-2} M_{\odot}$ . Hydrogen burning at the bottom of the deeply convective envelope eats its way outward into the envelope (solid line), producing helium that accumulates on top of the core. When this layer reaches a critical mass, helium burning ignites and forms the convective zone indicated by the vertically hatched area.

This zone grows rapidly and soon approaches the H-rich envelope, which is pushed outward due to the large energy production during the He shell flash. After He burning is completed, the envelope shrinks back and engulfs up to one third of the previous burning zone, and since it is fully convective, freshly synthesized *s*-process material is quickly cooled and dredged up to the surface (third dredge-up). While helium burning lasts for only about 200 yr, it takes about  $5 \cdot 10^4$  yr for hydrogen burning to replenish the consumed helium. These helium burning episodes can repeat about 20 to 30 times.

Neutron production and concordant *s* processing occur in two steps. During shell hydrogen burning, the  $^{13}\text{C}(\alpha, \text{n})^{16}\text{O}$  reaction is activated in the forming He layer. The  $^{13}\text{C}$  fuel is produced via the sequence



by protons penetrating the H-He interface by diffusion or semiconvection. This mixing mechanism and the amount of produced  $^{13}\text{C}$  (and of  $^{14}\text{N}$  by proton captures on  $^{13}\text{C}$ ) are crucial for a quantitative description of the resulting neutron exposure. Despite of first encouraging theoretical results [174,175] the formation of this  $^{13}\text{C}$  pocket is still treated in a parameterized way. For a full account of the related problems see Ref.[14].

The relatively low temperatures in the forming He layer of  $T_8 \sim 1$  are sufficient for producing a low neutron density of  $\approx 10^7 \text{ cm}^{-3}$  from this  $^{13}\text{C}$  pocket, which is, however, restricted to a very thin layer. Since the duration of the H burning phase is sufficiently long, the  $^{13}\text{C}$  is completely consumed, resulting in a large neutron exposure of the material in that layer. After the onset of the subsequent helium shell flash, this material is mixed with matter that has partly experienced previous neutron exposures.

At first glance, the above neutron densities and temperatures seem to contradict the results derived via the canonical approach (Sec. 4.2.2), where the branching analyses listed in Table 2 implied significantly larger values. This discrepancy is resolved when the second neutron source is considered, which becomes operational towards the end of the He shell flash when the maximum temperature of  $T_8 \sim 3$  is reached. The rather high peak neutron densities of more than  $10^{10} \text{ cm}^{-3}$  liberated via the  $^{22}\text{Ne}(\alpha, \text{n})^{25}\text{Mg}$  reaction are coupled to the high-temperature phase and last only for a short period of a few years (black intervals in Fig. 19). Though this second neutron source contributes not more than about 5% to the overall exposure and does, therefore, not alter the overall abundance distribution, it is still sufficient to adjust the isotopic patterns of the *s*-process branchings [176].

It is important to realize the dynamics of this second neutron burst. As illustrated in Fig. 20 the neutron density,  $n_n$ , lasts for only a few years, showing an almost instantaneous onset and also a rather steep decline. Because the peak temperature rises slightly from pulse to pulse, the overall exposure is clearly increasing with time and starts to be significant only from the 10th to 15th He shell flash. In view of the high peak neutron densities and the pronounced time-dependence of the flux, the abundance pattern in the critical branchings is obviously determined by the freeze-out at the end of the pulse rather than by characteristic *mean* conditions suggested by the superseded canonical model. Nevertheless, the delicate isotopic pattern of these branchings remains a most sensitive test, also for the advanced stellar *s*-process models.

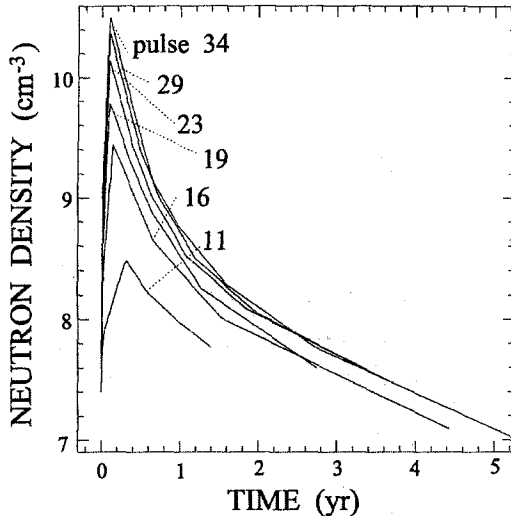


Fig. 20. The neutron density due to the  $^{22}\text{Ne}(\alpha, \text{n})^{25}\text{Mg}$  reaction for a number of subsequent He shell flashes in a star of 3 solar masses reflecting the rapid change of temperature during these intervals. It is this minor part of the overall neutron exposure that determines the isotopic pattern in the *s*-process branchings [176].

The difficulties in describing the stellar scenarios, in particular the mechanism for mixing of protons through the H-He interface, underline the role of the *s*-process abundances as an important tool for testing stellar models [142,176,177]. Fig. 21 shows the *s*-process overabundances relative to solar, which are accumulated in the envelope of a  $2 M_{\odot}$  AGB star with half the solar metallicity. This model appears to represent the solar *s* abundances quite well, all *s*-only nuclei (black diamonds) exhibiting practically the same enhancement. This is the more important since even those *s*-only nuclei are properly reproduced, which are partially bypassed by the reaction flow due to a nearby branching.

Another interesting feature is the relative deficiency of nuclei below  $A = 90$ . This solves the irritating problem in the analysis of the  $^{85}\text{Kr}$  branching, where the previous models had always led to an overproduction of the neutron-magic nuclei at  $N = 50$  [142].

It is to be emphasized, however, that the case of Fig. 21 is by no means representative of the solar composition, since the solar *s* abundances are an average over the Galactic evolution with contributions from many different stars. Variations of the metallicity, for example, have a strong effect on the total neutron exposure. In low metallicity stars, the *s* process operates more efficiently, because there are fewer neutron poisons. The increasing neutron exposure with decreasing metallicity bears the important consequence that in very metal-poor stars the *s* abundances are accumulating at  $^{208}\text{Pb}$  and

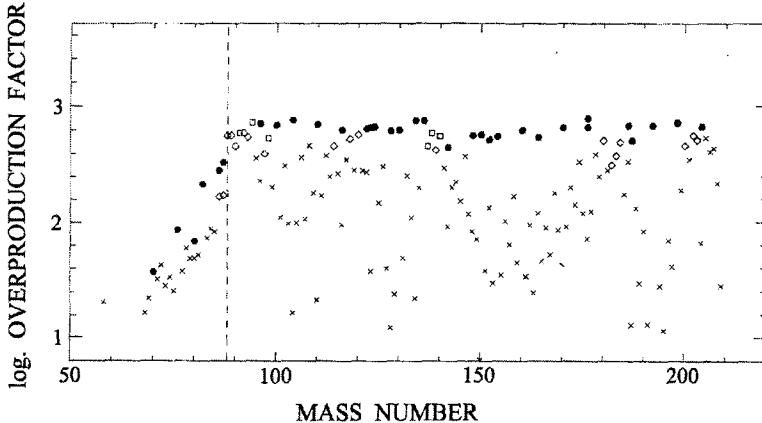


Fig. 21. Cumulative *s*-process enhancements in the envelope of a thermally pulsing AGB star ( $2M_{\odot}$ ,  $Z=0.01$ ). The almost constant overproduction of the *s*-only nuclei (black diamonds) shows that this particular star is representative for the solar main component [176].

$^{209}\text{Bi}$ , where the *s* process path terminates [176]. This behavior offers a natural explanation for the **strong** component originally suggested to explain the surplus of  $^{208}\text{Pb}$  that was not accounted for by the main *s* component [143]. The abundance pattern around  $^{208}\text{Pb}$  is also important for the  $^{235}\text{U}$  clock (Sec.6).

Despite of the problems in quantifying the stellar models for the red giant phase, it is quite obvious by now that realistic *s*-process scenarios differ completely from the assumption of a steady situation made in the canonical approach. Therefore, this solution is not suited to account for the significantly more complex stellar situations. This holds also for the recent attempts to complement the canonical model by means of a network code [144] or a parameterized analytic description [52] of the combined action of the pulsed  $^{13}\text{C}$  and  $^{22}\text{Ne}$  sources.

#### 4.3.2 Core helium burning in massive stars

Fairly soon after the **weak** component had been established, core helium burning in massive stars had been suggested as a promising stellar site [178–183]. While all the  $^{14}\text{N}$  produced in the CNO cycle during H burning is rapidly transformed into  $^{22}\text{Ne}$  at the very beginning of the He burning phase, it is only near He exhaustion in the core, that the central temperature rises sufficiently to ignite the  $^{22}\text{Ne}(\alpha, n)^{25}\text{Mg}$  reaction, thus providing the neutron source for the weak *s* component.

After these exploratory studies, a series of nucleosynthesis calculations has been performed with increasingly refined nuclear physics input and different

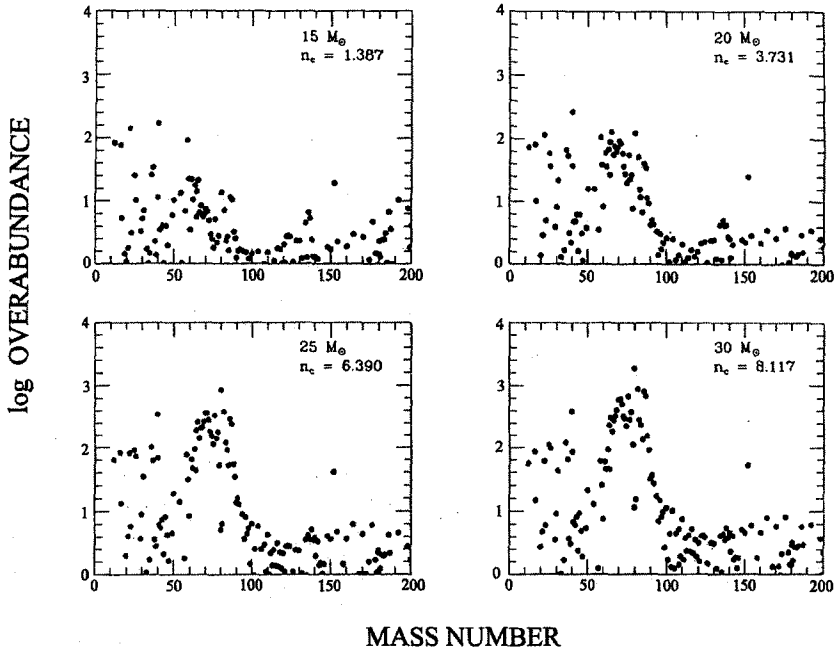


Fig. 22. The weak *s*-process component can be reproduced during core He burning in massive stars. This is shown by the overproduction factors obtained for a sequence of stars of solar metallicity. The number of captured neutrons per seed nucleus,  $n_c$ , indicates the *s*-process efficiency [93].

stellar models [147,148,184,185] to investigate the sensitivity to the nuclear physics input, the effect of different stellar models as well as the dependence on stellar mass and metallicity. In general, it was found that the weak component could be reproduced with model stars of  $20$  to  $30 M_\odot$  but that the efficiency decreases rapidly with decreasing stellar mass. For a series of stars with solar metallicity this decrease in efficiency is illustrated in Fig. 22 [93]. One finds that all these stars produce significant abundances in the mass range of the weak component, between  $A=60$  and  $90$ , and that all distributions are rather similar irrespective of their mass.

However, the weak component was not only produced by stars of solar metallicity. For a reasonable estimate it is, therefore, important to consider the contributions from the entire stellar population averaged over Galactic evolution. Accordingly, the effect of metallicity on the *s*-process yields has been studied in some detail [49,148,186].

Fig. 23 from Ref. [148] illustrates nicely that the *s*-process efficiency is considerably reduced at low metallicities but that the shape of the distribution is conserved. The reason for this behavior lies in the *secondary* nature of both

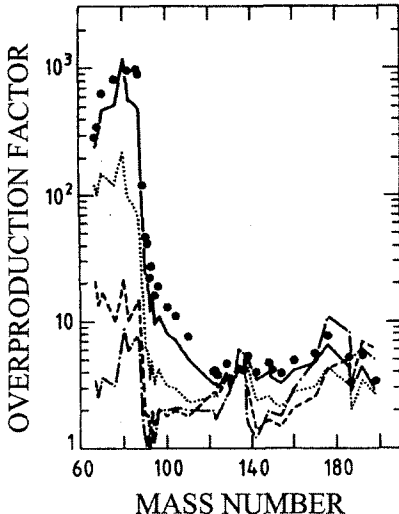


Fig. 23. The effect of metallicity on overproduction factors from the weak *s* process obtained during core He burning in a massive star with a core mass of  $10 M_{\odot}$  [148]. Metallicities have been varied from solar (dots) to  $10^{-4}$  solar (dashed-dotted line) in increments of 10.

the  $^{22}\text{Ne}(\alpha, \text{n})$  source and the seed nuclei. As the metallicity decreases, these secondary quantities decrease accordingly, whereas some of the very abundant isotopes, e.g.  $^{12}\text{C}$ ,  $^{16}\text{O}$ , which can be considered as neutron poisons, are *primary* nuclei produced within the star itself.

To some extent, the poisoning effect of  $^{12}\text{C}$  and  $^{16}\text{O}$  is eliminated in stellar He burning scenarios by the  $(\alpha, \text{n})$  reactions on the respective products  $^{13}\text{C}$  and  $^{17}\text{O}$ , which return the captured neutrons [187]. It was noted, however, that for  $^{16}\text{O}$  the recycling could be weakened at very low metallicities if the competing  $(\alpha, \gamma)$  reaction on  $^{17}\text{O}$  is strong enough [188].

In terms of nuclear physics uncertainties, this is not the only problem for stellar *s* processing. A major uncertainty has been identified for the crucial rate of the  $^{22}\text{Ne}(\alpha, \text{n})^{25}\text{Mg}$  reaction itself, which needs to be solved before stellar models of the weak component can be tested by comparison of the calculated and observed abundances [93].

The *s*-process efficiency in massive stars is not only determined during core He burning, but can also be affected by the subsequent shell C and Ne burning phases, when the  $^{22}\text{Ne}(\alpha, \text{n})$  source is reactivated [150,185]. Due to the higher temperatures, also the neutron density is much higher than during core He burning, leading to significant consequences for the *s*-process branchings at  $^{79}\text{Se}$  and  $^{85}\text{Kr}$ .

Despite of the successful reproduction of the weak component, stellar models are still left with a number of ambiguities and uncertainties. Some of these have been discussed with respect to the *s*-process yields, in particular the problem of modelling convection in the late stages of He burning and the modification or even destruction of the *s* abundances during subsequent phases of evolution [93]. Other important questions remain still to be investigated, for example the consequences of rotation, mass loss, and accretion in binary systems for the final *s*-process yields. In particular, rotation has been shown to have a dramatic effect on the evolution of massive stars [189,190], and it will be very interesting to see the corresponding impact on the weak component.

#### 4.4 Abundances: *s*-process yields and *r*-process residuals

With the now revealed limitations of the canonical *s*-process model and with the complexity of stellar *s*-process scenarios the quest for the *s*-process abundance distribution became suddenly more complicated.

***s*-Process Yields:** While the canonical model is still useful in mass regions where the cross sections are large enough that reaction flow equilibrium was established, it shows severe problems near magic nucleon numbers. This is certainly true around  $Z=50$  and  $N=82$ , where the *s*-only nuclei  $^{116}\text{Sn}$ ,  $^{136}\text{Ba}$ , and  $^{142}\text{Nd}$  (Sec. 4.2.3) were found to be inherently in error. Reasons, why the corresponding problems at  $N=50$  and  $N=128$  have not yet been identified, are persisting cross section uncertainties and the overlap of contributions from different *s*-process components.

Stellar *s*-process yields depend not only on the particular He-burning scenarios in low mass AGB stars or in massive stars but exhibit also large variations according to the stellar masses and metallicities. An attempt to obtain a representative *s*-process distribution by averaging the yields over the Galactic chemical evolution by Travaglio *et al.* [191] has shown an unexpected deficiency in the *s*-process yields between  $A=90$  and 120, which may require to reexamine the weak component.

Though it remains true that the isotopic *s* abundances are mostly determined by the respective cross sections, the very details of the distributions are more influenced by the complicated interplay between stellar temperatures and neutron fluxes than has been anticipated for a long time. This opens a most interesting perspective for stellar models, since these surprising abundance features are in general based on rather reliable nuclear physics data. Accordingly, the refined models can be sensitively tested via the associated *s*-process patterns.

***r*-Process Residuals:** The additional uncertainties in the *s*-process abundances, which originate from the complexity of the respective scenarios, prop-

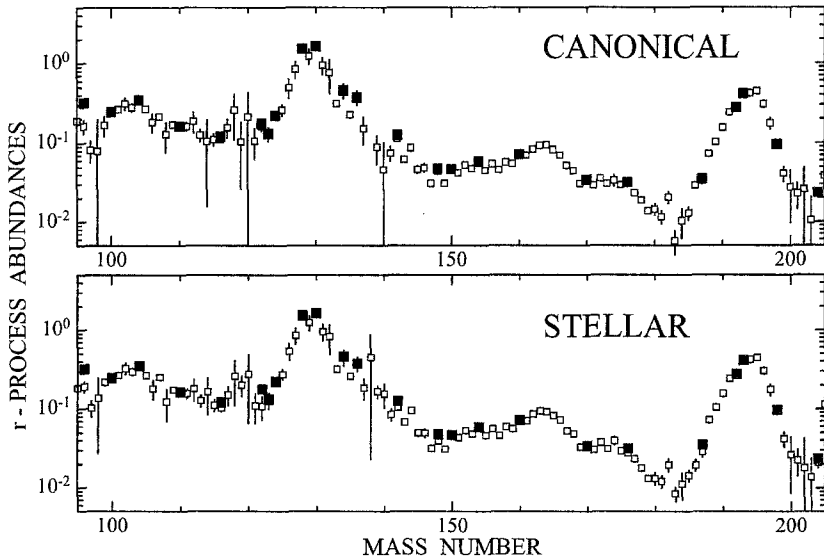


Fig. 24. The  $r$ -process abundances obtained as the differences between the solar and the  $s$  abundances,  $N_{\odot} - N_s$  (open circles) compared to the  $r$ -only nuclei (full squares). Top:  $s$  abundances from canonical model. Bottom:  $s$  abundances from stellar model, represented by the average yields from thermally pulsing AGB stars of  $1.5$  and  $3M_{\odot}$ .

aggregate also into the  $r$  distribution, since the usual decomposition of the solar abundances into their  $s$  and  $r$  components is simply obtained by the differences between the solar and the  $s$  abundances,

$$N_r = N_{\odot} - N_s.$$

However, these uncertainties are considerably damped wherever the  $r$  component dominates. Therefore, the resulting distributions are quite similar, regardless which  $s$ -process model was used, and match very well with the abundances of the  $r$ -only isotopes as shown in Fig. 24 [125]. In the top panel of Fig. 24 the  $r$  residuals have been obtained by subtracting the  $s$  abundances derived from the canonical model. For the stellar case (bottom panel) the  $s$  abundances are represented by the average distributions from  $1.5$  and  $3M_{\odot}$  stars [125].

In general, the  $r$  distribution provides, therefore, still a reliable basis for comparison with model calculations. Only in critical mass regions, for example at Pb/Bi or in the vicinity of magic numbers, the  $r$  distribution might be questioned. Note that Fig. 24 is not corrected for the residual  $p$ -process abundances, which are negligible in this context (at least in the mass region  $A > 100$ ). For numerical values of the  $r$  residuals see Refs. [13,52,192].

#### *4.5 Comparison with observations*

##### *4.5.1 The surface composition of AGB stars*

Ever since the 1952 discovery of *s*-process Tc by Merrill [4], the atmospheres of red giants remained a fascinating source of information for studies of stars on the asymptotic giant branch. Genuine enrichment by *s*-process material is common for the relatively cool MS, S, and N-type C stars with surface temperatures between 2800 and 3800 K, whereas the *s* enhancements in the hotter Ba stars are meanwhile understood as the result of mass overflow in binary systems [193,194].

Consequently, these MS, S, and C giants can be considered as the only live AGB stars undergoing He shell flashes with concomitant *s*-process nucleosynthesis. Though their low surface temperatures make them difficult to observe, modern observational techniques allow to study the surface compositions over a wide range of elements [42,172,195]. An impressive example for the remarkably detailed analyses based on these observations is the determination of the *s*-process neutron density for a sample of M, MS, and S giants [31].

In this work, carefully measured Rb/Sr abundance ratios as well as the isotopic patterns obtained from the ZrO molecular bands were used to constrain the *s*-process branchings at  $^{85}\text{Kr}$  and  $^{95}\text{Zr}$ . The resulting limits for the neutron density were found to be consistent with the expected value for the  $^{13}\text{C}(\alpha, \text{n})$  source, but significantly lower than the predictions for the higher fluxes from the  $^{22}\text{Ne}(\alpha, \text{n})$  reaction. This may reflect the gradual increase of the contribution from the  $^{22}\text{Ne}$  source along the AGB phase, according to the increase of temperature in subsequent convective He shell flashes (Fig. 20). For a test of this possibility it would, therefore, be important to enlarge the sample of AGB stars by further observations.

##### *4.5.2 Isotopic composition of presolar grains*

As outlined in Sec. 2, nucleosynthesis studies normally have to refer to the isotopic abundance distribution of solar material, which is best represented by the composition of primitive meteorites corresponding to that of the protosolar nebula [26,23].

Beyond that representative solar mix, the isolation of presolar grains from these meteorites has established a new field of "isotopic" astronomy. This exciting new access to the chemical abundance memory of nature [196–199] has attracted increasing interest from astrophysicists as well as from astronomers. These grains were identified to originate from circumstellar envelopes of mass-losing red giants and from supernova ejecta and have made their way through

the interstellar medium without modification. Therefore, they contain "pure" *s*- and *r*-process material and, hence, represent important probes for these objects that allow to study the corresponding nucleosynthesis processes in the most direct way.

A variety of grains have been found and isolated, e.g. micro-diamonds,  $\text{Si}_3\text{N}_4$ , and SiC-X from supernovae, SiC and corundum from AGB stars as well as graphite grains from both sources and from novae [199]. An illustrative example for the nuclear physics impact on these analyses are the isotopic anomalies for Ba and Nd, which were attributed to the *s* process but could not be described quantitatively [200] until accurate neutron capture data became available [159,201].

In particular, the *s*-process isotopic compositions carry very detailed information on the AGB phase. The example of the anomalous Kr patterns shown in Fig. 25 [14] provides evidence that the neutron density during the *s*-process exhibits indeed significant variations, which are obvious from the large scatter of the  $^{86}\text{Kr}$  component as a result of the branching at  $A=85$  mentioned in the previous section. A similar scatter has also been observed for  $^{96}\text{Zr}$  [202,203]. It is intriguing to fit these analyses to the information obtained from spectroscopy of the AGB star atmospheres and to see how the relative contributions from the neutron producing reactions on  $^{22}\text{Ne}$  and  $^{13}\text{C}$  can be traced from the activation of the branchings at  $^{85}\text{Kr}$  and  $^{95}\text{Zr}$ .

Since the anomalous isotope pattern can be measured very precisely, this information has to be complemented by accurate cross section data in order to achieve a full interpretation in an astrophysical sense. This requirement represents quite a challenge since many of the interesting elements, e.g. O, Mg, Si, Ca, Ti, Cr, and Zr fall in mass regions where typical  $(n,\gamma)$  cross sections are small. So far, such data are scarce and exhibit rather large uncertainties, a situation that deserves future efforts.

The rare earth elements are also of great interest in this respect. Though these are difficult to investigate because of their smaller abundances, their *s*-process patterns exhibit the signatures of pronounced branchings (Table 2) which are sensitive to relevant parameters of the stellar plasma (see Ref. [14] for a more complete discussion.)

## 5 Explosive scenarios and the *p* nuclei

While *s*-process nucleosynthesis accounts for about one half of the heavy element abundances, the other half is provided by processes occurring under explosive conditions, predominantly in supernovae. The very high tempera-

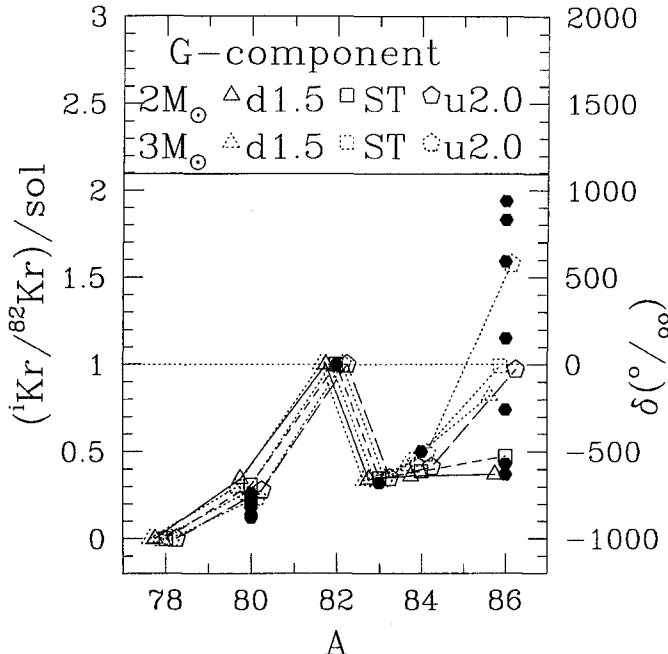


Fig. 25. Krypton isotope patterns in SiC dust grains from different meteorites [204] (solid symbols) compared to calculated isotope ratios of *s*-process krypton produced in the He-shell of 2 and 3  $M_{\odot}$  stars (open symbols) [14]. The calculated ratios refer to different assumptions for the contribution from the  $^{13}\text{C}(\alpha, \text{n})$  neutron source. The scatter of the  $^{86}\text{Kr}$  abundances implies that these dust grains originate from a variety of stellar masses and neutron exposures, thus indicating that the solar system *s*-process abundances are probably an average from many sources.

tures and densities in the nucleosynthesis zones result in reaction time scales which are much shorter than those for  $\beta$ -decay. Accordingly, explosive nucleosynthesis involves reactions on unstable and fairly short-lived nuclei which are difficult to study in the laboratory. Therefore, nuclear theory must be invoked for extrapolating the relevant properties of the known isotopes to the reaction paths far from stability. In addition to this uncertainty, the hydrodynamics of the explosion represents a difficult problem in itself. The attempt to reproduce the observed abundance patterns can, therefore, provide important clues for supernova models.

### 5.1 The *r*-process nucleosynthesis

Though the true *r*-process site is not yet completely settled, recent models concentrate on the high entropy, low density region behind the shock front in supernovae of type II [205,206]. This region is characterized by temperatures of  $T_9 \sim 1$  to 2 and very high neutron densities far in excess of  $10^{20} \text{ cm}^{-3}$ . Under

these conditions, a rapid sequence of  $(n,\gamma)$  reactions shifts the reaction path to extremely neutron rich nuclei, leading to an abundance distribution which includes even the heaviest naturally occurring nuclei in the actinide region (Fig. 24).

In terms of the heavy element abundances the  $r$  process may be considered as the counterpart to the  $s$  process, since it is responsible for almost all of the difference between the solar values and the  $s$ -process yields. For a full discussion of the various aspects of  $r$ -process nucleosynthesis the reader is referred to the contribution of Haxton and Qian in this volume.

## 5.2 The $p$ process

The most proton rich nuclei in Fig. 5 cannot be produced in any neutron capture process. The 32 stable isotopes of this category between  $^{74}\text{Se}$  and  $^{196}\text{Hg}$  are 10 to 100 times less abundant than the  $s$ - and  $r$ -process nuclei but exhibit a similar distribution. These nuclei are assumed to originate from the modification of an  $s$ - or  $r$ -seed in the  $p$  process, either by  $(p,\gamma)$  or photodisintegration reactions [15].

Possible sites for a  $(p,\gamma)$  origin appear not very promising, because novae are not efficient enough and Thorne-Żytkow objects [207] are still rather speculative. On the other hand, a  $\gamma$ -process in supernovae has been shown to reproduce the observed  $p$  abundances fairly well [49,208–210]. In the explosively burning O/Ne layers, typical temperatures of  $T_9 \sim 2 - 3$  are maintained for about 1 s at densities of  $\sim 10^6 \text{ g cm}^{-3}$ . Under these conditions, proton rich nuclei are produced by a sequence of five to ten  $(\gamma,n)$  reactions. When this sequence is halted by the increasing neutron separation energies, the reaction flow is dominated by  $(\gamma,p)$  and  $(\gamma,\alpha)$  channels.

In quantitative investigations, large reaction networks with  $\sim 1000$  nuclei and 10000 reactions have to be used as indicated by the shaded area in Fig. 26. Until recently, this entire mass region had been almost completely neglected by experimentalists, so that these studies had to rely on calculated data only. In fact, of the huge number of reactions only a single  $(p,\gamma)$  cross section for  $^{90}\text{Zr}$  [211], two  $(\alpha,\gamma)$  values for  $^{70}\text{Ge}$  and  $^{144}\text{Sm}$  [212,213], as well as a few  $(n,\gamma)$  rates for some stable  $p$  nuclei [73] had been measured before 1996.

Though most isotopes in the  $p$ -process network are unstable and, therefore, difficult to investigate, any information on stable  $p$  isotopes is valuable for testing the calculated Hauser-Feshbach rates near the stability valley. Such a test is shown in Fig. 27 for the example of the  $(n,\gamma)$  cross sections of the Er isotopes. The general importance of  $(n,\gamma)$  reactions during the freeze-out of the  $p$  abundance distribution has been emphasized in Ref. [214]. For extrapolat-

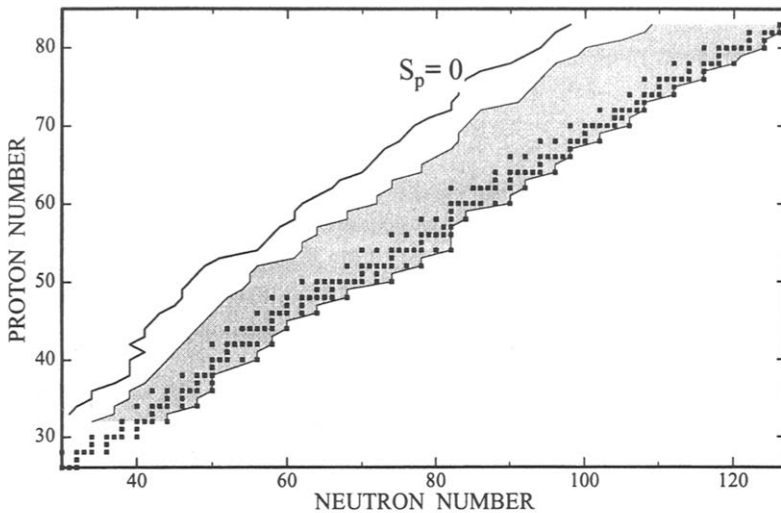


Fig. 26. The  $p$ -process network (shaded area). At the highest temperatures, the actual reaction path runs far from stability but approaches the stable nuclei (full circles) as the temperature decreases.

ing the neutron capture cross sections into the  $p$ -process region, all previously available data for the stable Er nuclei were used to adjust the parameters for the respective Hauser-Feshbach calculations [73,215]. However, improved measurements including the  $p$  isotope  $^{162}\text{Er}$  [151,216] require a modified extrapolation, resulting in two times larger cross sections in the  $p$ -process region. Accordingly, similar measurements over a broad mass region will certainly help to improve the parameter systematics for the Hauser-Feshbach calculations in the majority of unstable nuclei in the network, which remain inaccessible to laboratory techniques.

The dramatic lack of experimental data has meanwhile triggered a number of activities. Among the applied techniques, activation has been shown to be a particularly efficient and versatile tool not only for neutron capture measurements (Sec. 4.1.1) but also for the determination of  $(p, \gamma)$  and  $(\alpha, \gamma)$  cross sections [109]. It has been successfully used for an  $(\alpha, \gamma)$  measurement of the  $^{144}\text{Sm}$  cross section [213], for  $(p, \gamma)$  studies on a series of Mo and Ru isotopes [109,110] as well as for measurements on  $^{96}\text{Zr}$  and  $^{112,119}\text{Sn}$  [217]. However, in all cases where the reaction product is stable, the direct detection of the prompt capture  $\gamma$ -rays is the only alternative. An example for this more elaborate method are the  $^{70}\text{Ge}(\alpha, \gamma)^{74}\text{Se}$  cross section measurements of Fülöp *et al.* [212].

Despite of the uncertain nuclear physics,  $p$ -process models have been worked out in detail for SN II [49,208–210] and in a more schematic way for SN Ia [209]. It has to be considered a remarkable success that the observed abundances of the  $p$ -only nuclei can be reproduced within a factor of three by both approaches

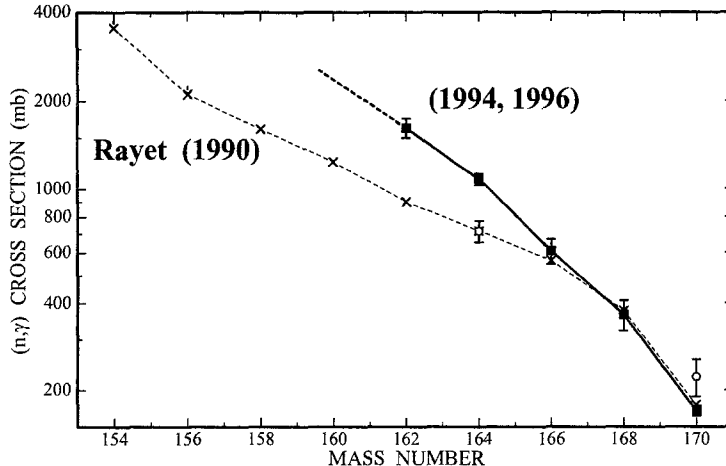


Fig. 27. New and improved  $(n,\gamma)$  cross sections of the even Er isotopes suggest a revision of Hauser-Feshbach calculations for the  $p$ -process network [215], which were adjusted to the previously available experimental data (open circles) [73].

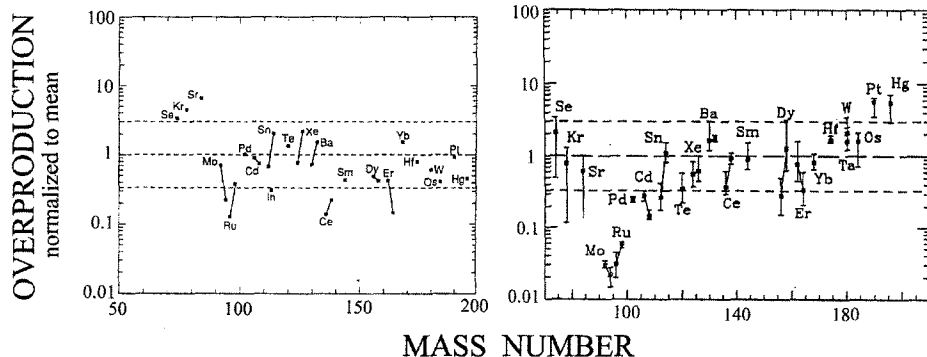


Fig. 28. The overproduction factors for the  $p$  abundances obtained with supernova models. Left panel: schematic SN Ia models [209], right panel: average for a range of detailed SN II models, the "error bars" indicating the possible variations for the investigated mass interval  $13$  and  $25 M_{\odot}$  [49].

(Fig. 28). However, both scenarios have problems in describing the light  $p$  nuclei with  $A < 100$  correctly. Since the  $p$  process in SNII is dominated by photodisintegrations from heavy seeds, this model does not account for the relatively large abundances of  $^{92}\text{Mo}$ ,  $^{94}\text{Mo}$ ,  $^{96}\text{Ru}$ , and  $^{98}\text{Ru}$ . In SNIa models, this deficiency is compensated by the fact that protons are released in carbon burning and captured by the abundant neutron magic isotopes with  $N=82$ , thus contributing the missing  $p$ -process Mo and Ru. However, this effect is also felt by the lighter  $p$  nuclei  $^{74}\text{Se}$ ,  $^{78}\text{Kr}$ , and  $^{84}\text{Sr}$  which are, therefore, all overproduced.

In view of these difficulties one might suspect that some fraction of the critical Mo and Ru isotopes could have been synthesized in other processes. These include mainly neutrino induced reactions in current *r*-process scenarios [218] as well as the *rp* process [20].

**The *rp* process:** Explosive hydrogen burning on the surface of accreting neutron stars (X-ray burster) have been known to yield abundance contributions up to the Fe group [219–221], the sequence of rapid proton captures being halted at  $^{56}\text{Ni}$  due to the strong photodisintegration reaction  $^{57}\text{Cu}(\gamma, \text{p})^{56}\text{Ni}$ . However, when sequential two-proton captures  $^{56}\text{Ni}(2\text{p}, \gamma)^{58}\text{Zn}$  were identified as a plausible possibility to bridge this gap at  $^{57}\text{Cu}$  [20], it was found that the *rp*-process chain could continue along the N=Z line up to iodine, providing some delayed energy production which may explain the time structure of actually observed bursts. So far, this situation depends to a large extent on the yet unknown nuclear physics input [21]. Provided that this can be confirmed and that the ejection efficiency of processed material from the neutron star is high enough, the *rp* process may, indeed, provide the excess in the abundances of the light Mo and Ru isotopes, which are difficult to understand via the *p* process in supernovae.

## 6 Nuclear chronometers

An ideal nuclear chronometer is expected to work unambiguously. It, therefore, should consist of an unstable isotope that is produced in well defined proportion with its daughter. After production, it should be quickly confined in a closed system where it decays freely. Under these conditions, the age of the system can be expressed in terms of the parent/daughter ratio. Carbon dating is a good approximation of an ideal nuclear clock, despite of problems with the  $^{14}\text{C}/^{12}\text{C}$  ratio changing as a function of time or by contamination with contemporary carbon [222].

Nuclear chronometers can either be analyzed by observing the disappearance of the parent nuclide, as for  $^{14}\text{C}$ , or by the appearance of the daughter, which may be favorable if the daughter belongs to a less abundant element. In the ideal case, the time interval  $\Delta t$  between production and observation follows from the decay law,

$$N_M^0 = N_M^* \times \exp(-\lambda \Delta t)$$

where  $N_M^0$  and  $N_M^*$  denote the abundance of the parent isotope at the time of observation and production, respectively.

In reality, practically all chronometers are complicated by the following problems.

- (i) The initial abundance of the parent nuclide is neither constant nor well defined in time. In case of the *s* process, for example, there are at least three different time scales, the  $10^6$  years of nucleosynthesis during the AGB phase of a particular star, the roughly  $10^{10}$  years of Galactic evolution, and the  $4.55 \times 10^9$  years since the formation of the solar system.
- (ii) The parent isotope is usually not confined inside a closed system. In the *s*-process example, freshly produced material is mixed with matter of different composition already at the stellar site and again during and after its ejection into the interstellar medium.
- (iii) Also the decay rate,  $\lambda$ , may be drastically changed under extreme conditions, turning a chronometer into a thermometer as in the case of  $^{176}\text{Lu}$  [136,137,152].

These difficulties do not allow for unbiased interpretations but require complex analyses that account for the respective nucleosynthesis scenarios within a general Galactic evolution model.

### 6.1 Time scales for the *s* process

As far as the *s* process is concerned [223], all unstable isotopes on the reaction path sketched in Fig. 5 can be understood as potential chronometers, provided they define a time scale corresponding to a significant quantity. The shortest possible time scale is related to the *neutron capture time* for an isotope  $A$ , and hence to the stellar neutron flux,  $n_n \times v_T$ :

$$\tau_{n(A)} = \frac{1}{\lambda_{n(A)}} = \frac{1}{n_n \times v_T \times \sigma_{(A)}}.$$

If the respective  $\beta$ -decay rate is comparable to  $\lambda_n$ , the abundance pattern of the developing branching in the reaction path reflects this time scale and provides a measure for the neutron density at the stellar site as outlined in Sec. 4.5 [31,224].

If the neutron capture time is comparable to the *duration of the neutron bursts* shown in Figs. 19 and 20, the abundance pattern of such a branching can be used to test the He-burning time scale, which gives rise to the second burst via the  $^{22}\text{Ne}$  neutron source. Suited branchings of this type could be those at  $^{85}\text{Kr}$  and  $^{95}\text{Zr}$  with neutron capture times of a few years. In these cases, the neutron flux dies out before reaction equilibrium is achieved. However, both branchings are difficult to analyze because of significant contributions from the weak *s*-process component or from the *r* process, and a satisfactory solution is still missing.

The *transport to the stellar surface* in the third dredge-up phase can be in-

vestigated by means of the observed Tc abundances [225–227]. The analyses of these observations have to consider that the terrestrial decay rate of  $^{99}\text{Tc}$  ( $t_{1/2} = 2.1 \times 10^5$  yr) is reduced to a few years at *s*-process temperatures [130,228], which implies that it is quickly cooled below 10<sup>8</sup> K after its production. A complementary, temperature-independent chronometer for the third dredge-up is  $^{93}\text{Zr}$ , which can be followed by the appearance of its daughter  $^{93}\text{Nb}$  [225].

The time scale for the *formation of the solar system* can, in principle, be inferred from the abundance patterns which are affected by the decay of nuclei with half-lives between 10<sup>5</sup> and 10<sup>7</sup> yr [229]. Quantitative studies based on isotopic anomalies, which have been discovered for various *s* nuclei, showed, however, that - apart from the complex scenarios for mixing and dilution - the predictions for several suited species produced in AGB stars, e.g.  $^{26}\text{Al}$ ,  $^{41}\text{Ca}$ ,  $^{60}\text{Fe}$ ,  $^{93}\text{Zr}$ , and  $^{107}\text{Pd}$  would meet the observations [230,231]. A comprehensive update of this discussion on the basis of the recently revised AGB model [232] can be found in Ref. [233].

Also  $^{205}\text{Pb}$  has been considered another potentially promising *s*-process chronometer [234], whereas  $^{53}\text{Mn}$ ,  $^{129}\text{I}$ , and  $^{182}\text{Hf}$  were found to result from the continuous pollution of interstellar matter by explosive nucleosynthesis in supernovae [233].

A number of attempts have been made to constrain the *cosmic time scale* via *s*-process abundances. In the course of these studies it turned out that the half-life of the most favorable case, i.e. the long-lived *s*-only isotope  $^{176}\text{Lu}$ , was strongly temperature-dependent, making it a sensitive thermometer rather than a cosmic clock [137,156] (Sec. 4.2.2). Also, the  $^{40}\text{K}$  [84] and  $^{87}\text{Rb}$  [235] chronometers were found to be very difficult to interpret since both nuclei are produced by at least two different processes. Therefore, analyses of cosmic time scales concentrate presently on the *r*-process chronometers related to the decay of the long-lived actinides and of  $^{187}\text{Re}$ .

## 6.2 Chronometers for explosive nucleosynthesis

A complete and detailed account of the various *r*-process chronometers has been given in the review by Cowan *et al.* [236], and it is certainly beyond the scope of this contribution to add any systematic updates.

However, it is interesting to see that the classical chronometers for the *r* process, which are based on the  $^{232}\text{Th}/^{238}\text{U}$  and the  $^{235}\text{U}/^{238}\text{U}$  ratios [237] and on the  $^{187}\text{Re}/^{187}\text{Os}$  pair [238] are presently being revived after many years of scepticism (see e.g. Ref. [239]). For both chronometers, persisting difficulties could be solved by major achievements in laboratory experiments and astronomical

observations.

After the nuclear physics problems concerning the stellar cross section enhancement of  $^{187}\text{Os}$  had been settled by series of accurate measurements and detailed calculations [85–88,120], and after the correction for the  $s$ -process contribution to  $^{187}\text{Re}$  had been determined [155], the enormous reduction of the  $^{187}\text{Re}$  half-life at stellar temperatures by bound state  $\beta$ -decay [130] had represented the essential obstacle for the Re/Os chronometer [240]. The breakthrough in this case was the experimental determination of the  $\beta$ -decay half-life of fully ionized  $^{187}\text{Re}$  ( $t_{1/2} = 32.9 \pm 2.0$  yr [139]), in good agreement with the predicted value of 14 yr [130]. Based on this information, the rate for the key transition in the stellar decay to  $^{187}\text{Os}$  can now be given reliably, thus allowing to treat the astration of  $^{187}\text{Re}$  in a quantitative way [140,241,242].

The important new aspect for the interpretation of the U/Th ratio comes from the observation of heavy element abundances from very metal-poor stars, both by ground based techniques and with the Hubble Space Telescope (see Refs. [33,243] for example). In the oldest stars, the heavy element pattern beyond Ba is clearly of pure  $r$ -process origin, and includes in one case the chronometer element Th [244,245]. By comparison of the solar Th/Eu ratio with the value measured in the star CS 22892-052, Cowan *et al.* [245] obtained an age estimate of  $15.2 \pm 3.7$  Gyr, independent of the yet uncertain site of the  $r$  process. Consideration of Galactic chemical evolution could imply a somewhat older age of  $17 \pm 4$  Gyr. Using newer and more accurate nuclear data in combination with a waiting point approximation  $r$ -process model, the age of CS 22892-052 was found to be  $15.6 \pm 4$  Gyr [246]. Though this value is in agreement with recent globular cluster age determinations based upon Hipparcos data [247], the remaining uncertainties need to be investigated by more observations of long-lived radioactive elements in other metal-poor halo stars as well as by further improvement of the related  $r$ -process calculations.

## 7 Open problems

Despite of considerable progress the general status of neutron capture nucleosynthesis is far from being mature. This is particularly true for the  $r$  process related to explosive scenarios, which is complicated by the twofold difficulty of modelling the dynamics of the explosion and of treating a huge reaction network by means of theoretically determined nuclear physics data. But also for the  $s$  process, which takes place during the He burning phases of stellar evolution, many questions are not yet answered. In this case, however, the nuclear physics input is beginning to reach a level of reliability, which allows to use the related nucleosynthesis for testing the underlying stellar models.

Nevertheless, further experimental efforts are definitely required in several fields: measurements of the stellar  $(n,\gamma)$  cross are still missing for a number of important Ge, Xe, and Pt isotopes and the accuracy of such data needs to be improved in several mass regions, particularly from Se to Cd and from Hf to Hg. Another lack of data exists for the lighter elements between C and Fe, which are important for analyzing the composition of presolar grains found in meteorites. High priority must be given to the determination of a complete set of accurate cross sections for the *s*-only isotopes and to the difficult measurements on the radioactive branch point nuclei. In addition, the neutron producing reactions for the *s* process have to be studied with much better sensitivity.

Apart from the improvement of the experimental cross sections, theoretical calculations remain indispensable. This holds not only for the cross sections of very short-lived branch point isotopes but also for the effect of thermally excited states. The corresponding stellar enhancement factors constitute significant corrections for the measured cross sections and have to be calculated with due consideration of the inelastic channels. After all, stellar  $\beta$ -decay represents another domain, where few experimental data are available, and where nuclear theory has to be invoked for reliable estimates of the influence of temperature and electron density.

Naturally, the ultimate goal of understanding *s*-process nucleosynthesis can only be achieved with complete stellar models and by following Galactic chemical evolution in detail. Also in this respect, there are promising developments, but a number of complicated problems related to the AGB phase are still waiting for a quantitative treatment, e.g. the mechanism for the formation of the  $^{13}\text{C}$  pocket at the boundary between the envelope and the  $^{12}\text{C}$ -rich helium layer, the general question of mixing in the envelope, and the description of the mass loss rate. Appropriate solutions of these problems will certainly benefit from the information and constraints derived from nucleosynthesis studies and refined astronomical observations.

### Acknowledgements

I would like to thank many colleagues, in particular C. Arlandini, M. Busso, R. Gallino, P.E. Koehler, B.E. Meyer, A. Mengoni, Y. Nagai, T. Rauscher, K. Takahashi, F.-K. Thielemann, M. Wiescher, and K. Wissak for stimulating discussions as well as for their help in correcting and proof-reading the manuscript.

## References

- [1] V. Goldschmidt, Norske Vidensk. Akad. Skr., Mat.–Naturv. Kl. IV (1937).
- [2] H. Suess and H. Urey, Rev. Mod. Phys. **28**, 53 (1956).
- [3] A. Cameron, Ap. J. **129**, 676 (1959).
- [4] P. Merrill, Science **115**, 484 (1952).
- [5] H. Bethe and C. Critchfield, Phys. Rev. **54**, 248 (1938).
- [6] C. von Weizsäcker, Physik. Zeitschrift **39**, 639 (1938).
- [7] H. Bethe, Phys. Rev. **55**, 103 (1939).
- [8] E. Burbidge, G. Burbidge, W. Fowler, and F. Hoyle, Rev. Mod. Phys. **29**, 547 (1957).
- [9] A. Cameron, Report CRL-41, A.E.C.L. Chalk River, Canada (1957).
- [10] G. Wallerstein *et al.*, Rev. Mod. Phys. **69**, 995 (1997).
- [11] B. Meyer, Annu. Rev. Astron. Astrophys. **32**, 153 (1994).
- [12] I. Baraffe *et al.* in *Nuclear Physics in Europe: Highlights and Opportunities*, edited by J. Vervier et al., Nuclear Physics European Collaboration Committee (1997); <http://quasar.physik.unibas.ch/nupec>.
- [13] F. Käppeler, H. Beer, and K. Wissak, Rep. Prog. Phys. **52**, 945 (1989).
- [14] R. Gallino, M. Busso, and M. Lugaro, in *Astrophysical Implications of the Laboratory Study of Presolar Material*, edited by T. Bernatowicz and E. Zinner (AIP, New York, 1997), p. 115.
- [15] D. Lambert, Astron. Astrophys. Rev. **3**, 201 (1992).
- [16] F.-K. Thielemann *et al.*, in *Nuclear and Particle Astrophysics*, edited by J. Hirsch and D. Page (Cambridge University Press, Cambridge, 1998), p. 27.
- [17] J. Cowan, F.-K. Thielemann, and J. Truran, Phys. Rep. **208**, 267 (1991).
- [18] D. Arnett, *Supernovae and Nucleosynthesis*, (Princeton University Press, Princeton, 1996).
- [19] E. Zinner, Ann. Rev. Earth Planet. Sci **26**, 147 (1998).
- [20] H. Schatz *et al.*, Physics Reports **294**, 167 (1998).
- [21] F. Käppeler, F.-K. Thielemann, and M. Wiescher, Ann. Rev. Nucl. Part. Sci. **48**, 175 (1998).
- [22] N. Grevesse, A. Noels, and A. Sauval, in *Cosmic Abundances*, Astronomical Society of the Pacific Conference Series, Vol. 99, edited by S. Holt and G. Sonneborn (BookCrafters, San Francisco, 1996), p. 117.

- [23] H. Palme and H. Beer, in *Landolt-Börnstein New Series, Group VI, Vol. VI/3a*, edited by O. Madelung (Springer, Berlin, 1993), p. 196.
- [24] H. Reeves, Rev. Mod. Phys. **66**, 193 (1994).
- [25] W. Hix and F.-K. Thielemann, Ap. J. **460**, 869 (1996).
- [26] E. Anders and N. Grevesse, Geochim. Cosmochim. Acta **53**, 197 (1989).
- [27] E. Anders and M. Ebihara, Geochim. Cosmochim. Acta **46**, 2363 (1982).
- [28] A. Cameron, Space Sci. Rev. **15**, 121 (1973).
- [29] P. De Bièvre and P. Taylor, Int. J. Mass Spectrom. Ion Phys. **123**, 149 (1993).
- [30] D. Lambert, in *Evolution of Stars: The Photospheric Abundance Connection*, edited by G. Michaud and A. Tutukov (Kluwer, Dordrecht, 1991), p. 299.
- [31] D. Lambert *et al.*, Ap. J. **450**, 302 (1995).
- [32] B. Edvardsson *et al.*, Astron. Astrophys. **275**, 101 (1993).
- [33] C. Sneden, J. Cowan, D. Burris, and J. Truran, Ap. J. **496**, 235 (1998).
- [34] D. Péquignot and J.-P. Baluteau, Astron. Astrophys. **283**, 593 (1994).
- [35] H. Habing, Astron. Astrophys. Rev. **7**, 97 (1996).
- [36] B. Savage and K. Sembach, Ann. Rev. Astron. Astrophys. **34**, 279 (1996).
- [37] E. Fürst, W. Reich, and B. Aschenbach, Astron. Astrophys. **319**, 655 (1997).
- [38] R. Diehl, in *Nuclear Astrophysics*, edited by M. Buballa, W. Nörenberg, J. Wambach, and A. Wirzba (GSI, Darmstadt, 1998), p. 234.
- [39] D. Clayton *et al.*, Ap. J. Lett. **399**, L14 (1992).
- [40] C. Dupraz *et al.*, Astron. Astrophys. **324**, 683 (1997).
- [41] B. Gustafsson, Ann. Rev. Astron. Astrophys. **27**, 701 (1989).
- [42] V. Smith and D. Lambert, Ap. J. **311**, 843 (1986).
- [43] A. Zook, Ap. J. **289**, 356 (1985).
- [44] P. Magain, Astron. Astrophys. **297**, 686 (1995).
- [45] W. Gacquer, in *Nuclei in the Cosmos V*, edited by N. Prantzos (Editions Frontières, Gif sur Yvette), in press.
- [46] J. Truran, Astron. Astrophys. **97**, 391 (1981).
- [47] W. Hillebrandt and P. Höflich, Rep. Prog. Phys. **52**, 1421 (1989).
- [48] E. Müller, in *Nuclear Astrophysics*, edited by M. Buballa, W. Nörenberg, and A. Wambach, J. Wirzba (GSI, Darmstadt, 1998), p. 153.

- [49] M. Rayet *et al.*, Astron. Astrophys. **298**, 517 (1995).
- [50] Y. Nagai *et al.*, Ap. J. **381**, 444 (1991).
- [51] P. Koehler *et al.*, Phys. Rev. C **54**, 1463 (1996).
- [52] H. Beer, F. Corvi, and P. Mutti, Ap. J. **474**, 843 (1997).
- [53] P. Koehler and F. Käppeler, in *Nuclear Data for Science and Technology*, edited by J. Dickens (American Nuclear Society, La Grange Park, Illinois, 1994), p. 179.
- [54] C. Rubbia *et al.*, Report CERN/LHC/98-02 (EET), CERN (1998) .
- [55] A. Murzin *et al.*, in *Capture Gamma-Ray Spectroscopy and Related Topics*, edited by G. Molnar, T. Belgia, and Zs. Révay (Springer, Berlin, 1997), p. 850.
- [56] M. Heil, F. Käppeler, M. Wiescher, and A. Mengoni, Ap. J. **507**, 997 (1998).
- [57] K. Wissak *et al.*, Nucl. Instr. Meth. A **292**, 595 (1990).
- [58] K. Wissak *et al.*, Phys. Rev. C **52**, 2762 (1995).
- [59] S. Jaag and F. Käppeler, Phys. Rev. C **53**, 2474 (1996).
- [60] T. Ohsaki *et al.*, Ap. J. **422**, 912 (1994).
- [61] M. Igashira *et al.*, Ap. J. **441**, L89 (1995).
- [62] M. Kazarnovsky *et al.*, Nucl. Phys. **A621**, 239c (1997).
- [63] H. Beer and F. Käppeler, Phys. Rev. C **21**, 534 (1980).
- [64] W. Ratynski and F. Käppeler, Phys. Rev. C **37**, 595 (1988).
- [65] F. Käppeler, A. Naqvi, and M. Al-Ouali, Phys. Rev. C **35**, 936 (1987).
- [66] W. Zhao and F. Käppeler, Phys. Rev. C **44**, 506 (1991).
- [67] H. Beer, Ap. J. **375**, 823 (1991).
- [68] F. Käppeler, K. Toukan, M. Schumann, and A. Mengoni, Phys. Rev. C **53**, 1397 (1996).
- [69] J. Meissner *et al.*, Phys. Rev. C **53**, 459 (1996).
- [70] H. Beer *et al.*, Nucl. Instr. Meth. A **337**, 492 (1994).
- [71] F. Käppeler, M. Wiescher, and P. Koehler, in *Workshop on the Production and Use of Intense Radioactive Beams at the Isospin Laboratory*, edited by J. D. Garrett (Joint Institute for Heavy Ion Research, Oak Ridge, 1992), p. 163.
- [72] S. Jaag and F. Käppeler, Phys. Rev. C **51**, 3465 (1995).
- [73] Z. Bao and F. Käppeler, Atomic Data Nucl. Data Tables **36**, 411 (1987).

- [74] H. Beer, F. Voß, and R. Winters, Ap. J. Suppl. **80**, 403 (1992).
- [75] Z. Bao *et al.*, (1999), in preparation.
- [76] T. Sanami *et al.*, Nucl. Instr. Meth. A **394**, 368 (1997).
- [77] P. Koehler and H. O'Brien, Phys. Rev. C **39**, 1655 (1989).
- [78] P. Koehler and S. Graff, Phys. Rev. C **44**, 2788 (1991).
- [79] H. Schatz *et al.*, Ap. J. **413**, 750 (1993).
- [80] H. Schatz *et al.*, Phys. Rev. C **51**, 379 (1995).
- [81] C. Wagemans, S. Druyts, and R. Barthelemy, in *Nuclei in the Cosmos III*, edited by M. Busso, R. Gallino, and C. Raiteri (American Institute of Physics, New York, 1995), p. 169.
- [82] C. Wagemans, R. Bieber, and P. Geltenbort, Phys. Rev. C **54**, 389 (1996).
- [83] R. Reifarth, K. Schwarz, and F. Käppeler, in *Nuclear Data for Science and Technology*, edited by G. Reffo, A. Ventura, and C. Grandi (SIF, Bologna, 1997), p. 1621.
- [84] H. Beer and R.-D. Penzhorn, Astron. Astrophys. **174**, 323 (1987).
- [85] R. Macklin, R. Winters, N. Hill, and J. Harvey, Ap. J. **274**, 408 (1983).
- [86] R. Hershberger *et al.*, Phys. Rev. C **28**, 2249 (1983).
- [87] R. Winters, R. Carlton, J. Harvey, and N. Hill, Phys. Rev. C **34**, 840 (1986).
- [88] R. Winters, R. Macklin, and R. Hershberger, Astron. Astrophys. **171**, 9 (1987).
- [89] H. Drotleff *et al.*, Ap. J. **414**, 735 (1993).
- [90] C. Brune, I. Licot, and R. Kavanagh, Phys. Rev. C **48**, 3119 (1993).
- [91] V. Harms, K.-L. Kratz, and M. Wiescher, Phys. Rev. C **43**, 2849 (1991).
- [92] H. Drotleff *et al.*, Z. Phys. A **338**, 367 (1991).
- [93] F. Käppeler *et al.*, Ap. J. **437**, 396 (1994).
- [94] U. Giesen *et al.*, Nucl. Phys. A **561**, 95 (1993).
- [95] U. Giesen *et al.*, Nucl. Phys. A **567**, 146 (1994).
- [96] W. Hauser and H. Feshbach, Phys. Rev. **78**, 366 (1952).
- [97] E. Vogt, Adv. Nucl. Phys. **1**, 261 (1969).
- [98] P. Hodgson, *Nuclear Reactions and Nuclear Structure*, (Clarendon Press, Oxford, 1971).
- [99] T. Rauscher, F.-K. Thielemann, and K.-L. Kratz, Phys. Rev. C **56**, 1613 (1997).

- [100] G. Reffo, in *Parameter Systematics for Statistical Theory Calculations of Neutron Reaction Cross Sections*, Report IAEA-SMR-43 (IAEA, Vienna, 1980), p. 205.
- [101] G. Reffo, F. Fabbri, K. Wissak, and F. Käppeler, Nucl. Sci. Engineering **80**, 630 (1982).
- [102] G. Reffo, F. Fabbri, K. Wissak, and F. Käppeler, Nucl. Sci. Engineering **83**, 401 (1983).
- [103] R. Winters *et al.*, Ap. J. **300**, 41 (1986).
- [104] A. Iljinov *et al.*, Nucl. Phys. **A543**, 517 (1992).
- [105] A. Ignatyuk, K. Istekov, and G. Smirenkin, Sov. J. Nucl. Phys. **29**, 450 (1979).
- [106] K. Langanke, Phys. Lett. B **438**, 235 (1998).
- [107] F.-K. Thielemann, M. Arnould, and J. Truran, in *Advances in Nuclear Astrophysics*, edited by E. Vangioni-Flam *et al.* (Editions Frontières, Paris, 1986), p. 525.
- [108] T. Rauscher and F.-K. Thielemann, in *Atomic and Nuclear Astrophysics*, edited by A. Mezzacappa (IOP, Bristol, 1998), p. 519.
- [109] T. Sauter and F. Käppeler, Phys. Rev. C **55**, 3127 (1997).
- [110] J. Bork, H. Schatz, F. Käppeler, and T. Rauscher, Phys. Rev. C **58**, 524 (1998).
- [111] T. Rauscher, in *Nuclear Astrophysics*, edited by M. Buballa, W. Nörenberg, and A. Wambach, J. Wirzba (GSI, Darmstadt, 1998), p. 288.
- [112] C. Grama, in *Nuclei in the Cosmos V*, edited by N. Prantzos (Editions Frontières, Gif sur Yvette), in press.
- [113] S. Goriely, in *Nuclei in the Cosmos V*, edited by N. Prantzos (Editions Frontières, Gif sur Yvette), in press.
- [114] G. Mathews, A. Mengoni, F.-K. Thielemann, and W. Fowler, Ap. J. **270**, 740 (1983).
- [115] E. Krausmann *et al.*, Phys. Rev. C **53**, 469 (1996).
- [116] J. Holmes, S. Woosley, W. Fowler, and B. Zimmerman, Atomic Data and Nucl. Data Tables **18**, 305 (1976).
- [117] S. Woosley, W. Fowler, J. Holmes, and B. Zimmerman, Atomic Data Nucl. Data Tables **22**, 371 (1978).
- [118] R. Firestone, in *Nuclei in the Cosmos V*, edited by N. Prantzos (Editions Frontières, Gif sur Yvette), in press.
- [119] T. Rauscher, private communication (unpublished).
- [120] M. McEllistrem *et al.*, Phys. Rev. C **40**, 591 (1989).

- [121] F. Voss, K. Wissak, and F. Käppeler, Phys. Rev. C **52**, 1102 (1995).
- [122] P. Mutti, F. Corvi, K. Athanassopoulos, and H. Beer, Nucl. Phys. **A621**, 262c (1997).
- [123] K. Wissak *et al.*, Phys. Rev. C **48**, 1401 (1993).
- [124] P. Koehler *et al.*, Phys. Rev. C **57**, R1558 (1998).
- [125] C. Arlandini *et al.*, in *Nuclei in the Cosmos V*, edited by N. Prantzos (Editions Frontières, Gif sur Yvette), in press.
- [126] F. Käppeler, in *Radioactive Nuclear Beams*, edited by T. Delbar (Adam Hilger, Bristol, 1992), p. 305.
- [127] A. Cameron, Ap. J. **130**, 452 (1959).
- [128] J. Bahcall, Phys. Rev. **124**, 495 (1961).
- [129] J. Bahcall, Ap. J. **139**, 318 (1964).
- [130] K. Takahashi and K. Yokoi, Atomic Data Nucl. Data Tables **36**, 375 (1987).
- [131] N. Klay and F. Käppeler, Phys. Rev. C **38**, 295 (1988).
- [132] E. Sugarbaker, in *Nuclei in the Cosmos III*, edited by M. Busso, R. Gallino, and C. Raiteri (AIP, New York, 1995), p. 135.
- [133] C. Goodman *et al.*, Phys. Rev. Lett. **44**, 1755 (1980).
- [134] T. Taddeucci *et al.*, Nucl. Phys. **A469**, 125 (1987).
- [135] K. Pham *et al.*, Phys. Rev. C **51**, 526 (1995).
- [136] N. Klay *et al.*, Phys. Rev. C **44**, 2801 (1991).
- [137] N. Klay, F. Käppeler, H. Beer, and G. Schatz, Phys. Rev. C **44**, 2839 (1991).
- [138] M. Jung *et al.*, Phys. Rev. Lett. **69**, 2164 (1992).
- [139] F. Bosch *et al.*, Phys. Rev. Lett. **77**, 5190 (1996).
- [140] T. Faestermann, T. Takahashi, P. Kienle, and F. Bosch, in *Nuclear Astrophysics*, edited by M. Buballa, W. Nörenberg, and A. Wambach, J. Wirsba (GSI, Darmstadt, 1998), p. 417.
- [141] P. Seeger, W. Fowler, and D. Clayton, Ap. J. Suppl. **97**, 121 (1965).
- [142] F. Käppeler *et al.*, Ap. J. **354**, 630 (1990).
- [143] D. Clayton and M. Rassbach, Ap. J. **148**, 69 (1967).
- [144] S. Jaag, master thesis, University of Karlsruhe (1990).
- [145] S. Goriely, Astron. Astrophys. **327**, 845 (1997).

- [146] S. Goriely, in *Nuclear Astrophysics*, edited by M. Buballa, W. Nörenberg, J. Wambach, and A. Wirzba (GSI, Darmstadt, 1998), p. 320.
- [147] N. Langer, J.-P. Arcoragi, and M. Arnould, Astron. Astrophys. **210**, 187 (1989).
- [148] N. Prantzos, M. Hashimoto, and K. Nomoto, Astron. Astrophys. **234**, 211 (1990).
- [149] M. El Eid and I. Baraffe, in *Nuclei in the Cosmos*, edited by H. Oberhummer and W. Hillebrandt (MPI für Physik und Astrophysik, Garching, 1990), p. 238.
- [150] C. Raiteri *et al.*, Ap. J. **419**, 207 (1993).
- [151] S. Jaag and F. Käppeler, Ap. J. **464**, 874 (1996).
- [152] C. Doll, H. Börner, S. Jaag, and F. Käppeler, Phys. Rev. C **59**, 492 (1999).
- [153] F. Käppeler, W. Schanz, K. Wissak, and G. Reffo, Ap. J. **410**, 370 (1993).
- [154] F. Voss *et al.*, Phys. Rev. C **50**, 2582 (1994).
- [155] F. Käppeler, S. Jaag, Z. Bao, and G. Reffo, Ap. J. **366**, 605 (1991).
- [156] K. Lesko *et al.*, Phys. Rev. C **44**, 2850 (1991).
- [157] H. Beer, G. Walter, and R. Macklin, in *Capture Gamma-Ray Spectroscopy and Related Topics*, edited by S. Raman (AIP, New York, 1985), p. 778.
- [158] K. Wissak *et al.*, Phys. Rev. C **54**, 1451 (1996).
- [159] K. Wissak *et al.*, Phys. Rev. C **57**, 391 (1998).
- [160] J. Bahcall *et al.*, Rev. Mod. Phys. **54**, 767 (1982).
- [161] A. Weigert, Z. Astrophys. **64**, 395 (1966).
- [162] M. Schwarzschild and R. Härm, Ap. J. **150**, 961 (1967).
- [163] R. Ulrich, in *Explosive Nucleosynthesis*, edited by D. Schramm and D. Arnett (University of Texas, Austin, 1973), p. 139.
- [164] I. Iben Jr., Ap. J. **196**, 525 (1975).
- [165] I. Iben Jr., Ap. J. **196**, 549 (1975).
- [166] I. Iben Jr., Ap. J. **217**, 788 (1977).
- [167] I. Iben Jr. and J. Truran, Ap. J. **220**, 980 (1978).
- [168] K. Cosner, I. Iben Jr., and J. Truran, Ap. J. Lett. **238**, L91 (1980).
- [169] W. Howard, G. Mathews, K. Takahashi, and R. Ward, Ap. J. **309**, 633 (1986).
- [170] S. Little, I. Little-Marenin, and W. Hagen-Bauer, Astron. Journ. **93**, 1539 (1987).

- [171] I. Iben Jr. and A. Renzini, *Ann. Rev. Astron. Astrophys.* **21**, 271 (1983).
- [172] V. Smith and D. Lambert, *Ap. J. Suppl.* **72**, 387 (1990).
- [173] M. Busso *et al.*, *Ap. J.* **399**, 218 (1992).
- [174] F. Herwig, T. Blöcker, D. Schönberner, and M. El Eid, *Astron. Astrophys.* **324**, L81 (1997).
- [175] H. Singh, I. Roxburgh, and K. Chan, *Astron. Astrophys.* **340**, 178 (1998).
- [176] R. Gallino *et al.*, *Ap. J.* **497**, 388 (1998).
- [177] R. Gallino, in *The Evolution of Peculiar Red Giants*, edited by H. Johnson and B. Zuckerman (Cambridge University Press, Cambridge, 1989), p. 176.
- [178] J. Peters, *Ap. J.* **154**, 225 (1968).
- [179] R. Couch, A. Schmiedekamp, and D. Arnett, *Ap. J.* **190**, 95 (1974).
- [180] S. Lamb, W. Howard, J. Truran, and I. Iben, Jr., *Ap. J.* **217**, 213 (1977).
- [181] D. Arnett and F.-K. Thielemann, *Ap. J.* **295**, 589 (1985).
- [182] M. Busso and R. Gallino, *Astron. Astrophys.* **151**, 205 (1985).
- [183] N. Prantzos, M. Arnould, and J.-P. Arcoragi, *Ap. J.* **315**, 209 (1987).
- [184] C. Raiteri *et al.*, *Ap. J.* **367**, 228 (1991).
- [185] C. Raiteri, M. Busso, R. Gallino, and G. Picchio, *Ap. J.* **371**, 665 (1991).
- [186] C. Raiteri, R. Gallino, and M. Busso, *Ap. J.* **387**, 263 (1992).
- [187] C. Travaglio, R. Gallino, C. Arlandini, and M. Busso, *Memorie della Società Astronomica Italiana* **67**, 831 (1996).
- [188] M. Rayet and M. Hashimoto, in *Tours Symposium on Nuclear Physics III*, edited by M. Arnould *et al.* (AIP, New York, 1998), p. 605.
- [189] N. Langer, J. Fliegner, A. Heger, and S. Woosley, *Nucl. Phys.* **A621**, 457c (1997).
- [190] N. Langer, A. Heger, and H. Braun, in *Stellar Evolution, Stellar Explosions and Galactic Chemical Evolution*, edited by A. Mezzacappa (IOP, Bristol, 1998), p. 377.
- [191] C. Travaglio *et al.*, in *Nuclei in the Cosmos V*, edited by N. Prantzos (Editions Frontières, Gif sur Yvette), in press.
- [192] C. Arlandini *et al.*, in preparation.
- [193] R. McClure, *Ap. J.* **280**, 231 (1984).
- [194] E. Böhm-Vitense, J. Nemec, and C. Proffitt, *Ap. J.* **278**, 726 (1984).
- [195] V. Smith and D. Lambert, *Ap. J.* **294**, 294 (1985).

- [196] E. Anders and E. Zinner, Meteoritics **28**, 490 (1993).
- [197] U. Ott, Nature **364**, 25 (1993).
- [198] E. Zinner, Science **271**, 41 (1996).
- [199] S. Amari and E. Zinner, Nucl. Phys. A **621**, 99c (1997).
- [200] R. Gallino, C. Raiteri, and M. Busso, Ap. J. **410**, 400 (1993).
- [201] K. Guber, R. Spencer, P. Koehler, and R. Winters, Phys. Rev. Lett. **78**, 2704 (1997).
- [202] G. Nicolussi *et al.*, Science **277**, 1281 (1997).
- [203] G. Nicolussi *et al.*, Ap. J. **504**, 492 (1998).
- [204] R. Lewis, S. Amari, and E. Anders, Geochim. Cosmochim. Acta **58**, 471 (1994).
- [205] S. Woosley *et al.*, Ap. J. **433**, 229 (1994).
- [206] K. Takahashi, J. Witti, and H.-T. Janka, Astron. Astrophys. **286**, 857 (1994).
- [207] G. Biehle, Ap. J. **380**, 167 (1991).
- [208] N. Prantzos, M. Hashimoto, M. Rayet, and M. Arnould, Astron. Astrophys. **238**, 455 (1990).
- [209] W. Howard, B. Meyer, and S. Woosley, Ap. J. **373**, L5 (1991).
- [210] M. Arnould, S. Goriely, and M. Rayet, in *Nuclear Astrophysics*, edited by M. Buballa, W. Nörenberg, J. Wambach, and A. Wirzba (GSI, Darmstadt, 1998), p. 279.
- [211] C. Laird, D. Flynn, R. Hershberger, and F. Gabbard, Phys. Rev. C **35**, 1265 (1987).
- [212] Z. Fülöp *et al.*, Z. Phys. A **355**, 203 (1996).
- [213] E. Somorjai *et al.*, Nucl. Phys. A **621**, 293c (1997).
- [214] M. Rayet, N. Prantzos, and M. Arnould, Astron. Astrophys. **227**, 271 (1990).
- [215] M. Rayet, private communication (unpublished).
- [216] J. Best, Report, FZKA-5824, Forschungszentrum Karlsruhe (1996).
- [217] A. Murphy and et al., in *Nuclei in the Cosmos V* (Editions Frontières, Gif sur Yvette), in press.
- [218] G. Fuller and B. Meyer, Ap. J. Suppl. **48**, 279 (1982).
- [219] R. Wallace and S. Woosley, Ap. J. Suppl. **45**, 389 (1981).
- [220] R. Taam, Ann. Rev. Nucl. Sci. **35**, 1 (1985).
- [221] R. Taam, S. Woosley, T. Weaver, and D. Lamb, Ap. J. **413**, 324 (1993).

- [222] R. Hedges and J. Gowlett, *Scientific American* **254**, 82 (1986).
- [223] F. Käppeler, in *Nuclei in the Cosmos*, edited by H. Oberhummer (Springer, Berlin, 1991), p. 179.
- [224] K. Toukan, K. Debus, F. Käppeler, and G. Reffo, *Phys. Rev. C* **51**, 1540 (1995).
- [225] G. Mathews, K. Takahashi, R. Ward, and W. Howard, *Ap. J.* **302**, 410 (1986).
- [226] V. Smith and D. Lambert, *Ap. J.* **333**, 219 (1988).
- [227] M. Busso *et al.*, *Ap. J.* **446**, 775 (1995).
- [228] G. Schatz, *Astron. Astrophys.* **122**, 327 (1983).
- [229] A. Cameron, in *Protostars and Planets III*, edited by E. Levy and J. Lunine (Univ. Arizona Press, Tucson, 1993), p. 47.
- [230] G. Wasserburg, M. Busso, R. Gallino, and C. Raiteri, *Ap. J.* **424**, 412 (1994).
- [231] G. Wasserburg *et al.*, *Ap. J.* **440**, L101 (1995).
- [232] O. Straniero *et al.*, *Ap. J.* **440**, L85 (1995).
- [233] M. Busso, R. Gallino, and G. Wasserburg, *Ann. Rev. Astron. Astrophys.*, in press.
- [234] K. Yokoi, K. Takahashi, and M. Arnould, *Astron. Astrophys.* **145**, 339 (1985).
- [235] H. Beer and R.-D. Penzhorn, *Astrophys. Space Sci.* **100**, 234 (1984).
- [236] J. Cowan, F.-K. Thielemann, and J. Truran, *Ann. Rev. Astron. Astrophys.* **29**, 447 (1991).
- [237] W. Fowler and F. Hoyle, *Ann. Phys.* **10**, 280 (1960).
- [238] D. Clayton, *Ap. J.* **139**, 637 (1964).
- [239] B. Pagel, in *Astrophysical Ages and Dating Methods*, edited by E. Vangioni-Flam, M. Cassé, J. Audouze, and J. Tran Thanh Van (Editions Frontières, Gif sur Yvette, 1990), p. 493.
- [240] K. Yokoi, K. Takahashi, and M. Arnould, *Astron. Astrophys.* **117**, 65 (1983).
- [241] K. Takahashi, in *Tours Symposium on Nuclear Physics III*, edited by M. Arnould *et al.* (AIP, New York, 1998), p. 616.
- [242] P. Kienle, in *Nuclei in the Cosmos V*, edited by N. Prantzos (Editions Frontières, Gif sur Yvette), in press.
- [243] J. Cowan, C. Sneden, J. Truran, and D. Burris, in *Stellar Evolution, Stellar Explosions and Galactic Chemical Evolution*, edited by A. Mezzacappa (Institute of Physics, Bristol, 1998), p. 621.
- [244] C. Sneden *et al.*, *Ap. J.* **467**, 819 (1996).

- [245] J. Cowan, A. McWilliam, C. Sneden, and D. Burris, *Ap. J.* **480**, 246 (1997).
- [246] J. Cowan *et al.*, *Ap. J.* , submitted.
- [247] F. Pont, M. Mayor, C. Turon, and D. Vandenberg, *Ap. J.* , in press.